Development and fluctuation of crystal orientation fabric in the deep sections of the Dome Fuji ice core, Antarctica: impacts of dust particles and migration recrystallization

Tomotaka Saruya[1], Atsushi Miyamoto[2], Shuji Fujita[1,3], Kumiko Goto-Azuma[1,3], Motohiro Hirabayashi[1], Akira Hori[4], Makoto Igarashi[1], Yoshinori Iizuka[5], Takao Kameda[4], Hiroshi Ohno[4], Wataru Shigeyama[3*], Shun Tsutaki[1,3]

[1] National Institute of Polar Research, Tokyo 190-8518, Japan
[2] Institute for the Advancement of Graduate Education, Hokkaido University, Sapporo 060-0817, Japan
[3] Polar Science Program, Graduate Institute for Advanced Studies, SOKENDAI, Tokyo 190-8518, Japan
[4] Kitami Institute of Technology, Kitami 090-8507, Japan
[5] Institute of Low Temperature Science, Hokkaido University, Sapporo 060-0819, Japan

*Currently at: JEOL Ltd., Tokyo, Japan

Correspondence: Tomotaka Saruya (saruya.tomotaka@nipr.ac.jp), Atsushi Miyamoto (miyamoto@high.hokudai.ac.jp), Shuji Fujita (sfujita@nipr.ac.jp)

Added (or partially modified)

Removed

This study investigated the crystalline textural properties of an Antarctic deep ice core having a length of 3035 m acquired at an inland plateau dome, with a focus on depths below 2400 m. The cluster strength of the c-axes was ascertained using the dielectric tensor method to assess the bulk properties of thick sections and detailed orientation distributions of c- and a-axes were determined using the Laue X-ray diffraction technique. The c- and a-axes fabric data were compared with various other characteristics of the same ice core. Microstructural observations were made using optical microscopy. The clustering strength of the single-pole c-axis fabric was at a maximum at depths between 2400 and 2640 m. The relationship between cluster strength and the concentration of dusty impurities was found to change at approximately 2640 m and fluctuations in strength increased significantly below this depth. Impurity-rich layers maintained a high degree of clustering whereas layers having fewer impurities showed relaxation. The latter layers also exhibited bulging evidence of nucleation and grain boundary migration. In ice such as this, the degree of a-axis organization was increased with one or two sets of three preferred orientations. Dynamic recrystallization evidently played a critical role, with more pronounced effects in impurity-poor layers than in impurity-rich layers. This phenomenon promoted the relaxation of the c-axis clustering, deformation based on dislocation creep and organization of the a-axis. Below 2580 m, the angles of inclination of the c-axes cluster and layers were significantly deviated from the vertical, suggesting the system rotated as a rigid body as a result of simple shear.

1. Introduction

Crystal orientation fabric is one of the most important factors controlling the physical properties of polar ice sheets. In particular, both the deformation and flow of ice sheets are significantly affected by the crystal orientation fabric and the deformation response of individual ice crystals to stress exhibits pronounced anisotropy. Specifically, these crystals readily undergo shearing along the slip systems within their basal planes, whereas nearly a hundred times greater shear stress must be applied to induce deformation along other slip systems within the crystals (e.g., Duval et al., 1983). In the case that ice crystals are randomly oriented, these crystals will behave isotropically while nonrandom orientations will result in anisotropic behaviour. As an example, the internal deformation of an ice sheet can lead to the preferred orientation of ice crystals that, in turn, affects the flow of the sheet. The ice flow is also affected by the concentrations of ionic species and dust particles as well as by disturbances or folds in the layer structure (e.g., Cuffey and Paterson, 2010, Durand et al., 2007, Saruya et al., 2022b). These factors can introduce either positive or negative feedback that modulates the flow characteristics of the ice sheet. Considering this complexity, it is evident that a systematic understanding of the internal layered structure of polar ice sheets is required.

The rheology in the deepest several hundred meters of an ice sheet is complicated by geothermal effects and increased stresses resulting from the bedrock topography. Even so, to date, there have been limited reports concerning the crystal properties of ice near the bed at central plateau dome summits of ice sheets (e.g., Thorsteinsson et al., 1997; Durand et al., 2009, Faria et al., 2014a, Ohno et al., 2016). Deep ice is characterized by higher temperatures at which enhanced phenomena related to molecular transport becomes important (e.g., Petrenko and Whitworth, 1999). These phenomena include plastic deformation, molecular diffusion processes and recrystallization, and studies concerning dynamic recrystallization in ice sheets have been performed (e.g., Poirier 1985; De La Chapelle et al. 1998; Humphreys and Haterly 2004; Weikusat et al. 2009; Kipfstuhl et al. 2009; Montagnat et al. 2012, 2014; Faria et al., 2014a and Stoll et al., 2021a). The work reported herein took advantage of the unique opportunity that the Dome Fuji (DF) ice core offers with regard to assessing the role of dynamic recrystallization in the formation of textures and fabrics in the deeper parts of the East Antarctic ice sheet.

The crystal orientation fabric contains information concerning the history of deformation, grain growth and recrystallization (e.g., Cuffey and Paterson, 2010; Faria et al., 2014a, b). Saruya et al. (2022b) investigated the development of the c-axis fabric in the DF ice core at depths above 2400 m using thick sections of ice (ranging in thickness from 33 to 79 mm) in conjunction with radio wave birefringence. Using the dielectric tensor method (DTM), this prior work assessed the degree of dielectric anisotropy ($\Delta\varepsilon$) along ice cores. This parameter is defined as the difference in relative permittivity along the vertical (ε_v) and horizontal planes (ε_h), such that $\Delta\varepsilon = \varepsilon_v - \varepsilon_h$, and indicates the clustering strength of the c-axes. The value of $\Delta\varepsilon$ is linearly compatible with the normalized eigenvalues of the second order tensor (Saruya et al., 2022a, b). These authors also found that $\Delta\varepsilon$ steadily increases with depth but also exhibits fluctuations. In addition, significant decreases in $\Delta\varepsilon$ were identified at depths associated with major glacial-to-interglacial transitions. These observed changes in $\Delta\varepsilon$ can be explained by variations in the deformational history of regions of the ice sheet over which vertical compression is the primary cause of stress. The $\Delta\varepsilon$ data have additionally been shown to positively correlate with the concentration of chloride ions in the ice and inversely correlate with the amount of dust particles. Since both chloride ions and dust originate from atmospheric deposition, Saruya et al. (2022b) proposed that fluctuations in clustering strength might be common across wide areas of ice sheets.

On this basis, the present research studied the deepest 20% of the DF core (specifically, the depth range of 2400–3035 m) to provide a more complete understanding of the development of texture and fabric throughout the entire ice sheet column. A major challenge to this work was the inclination of the ice sheet layers, which becomes steeper at deeper depths (Dome Fuji Ice Core Project Members (DFICPM), 2017). This research utilized the DTM in conjunction with thick sections together with techniques utilizing thin sections, including the Laue X-ray diffraction method and microstructural observations. The textural data obtained with these methods is compared herein with various datasets produced from prior

studies of the same ice core. This paper provides an advanced, updated dataset concerning the crystal orientation fabric with regard to both the *c*-axis and *a*-axis along with additional textural data for the DF ice core. Using these data, the development of the crystal orientation fabric as well as variations in the microstructure, layered structure and rheology of polar ice sheets is discussed. This new information increases our understanding of the development of layered structures in ice sheets.
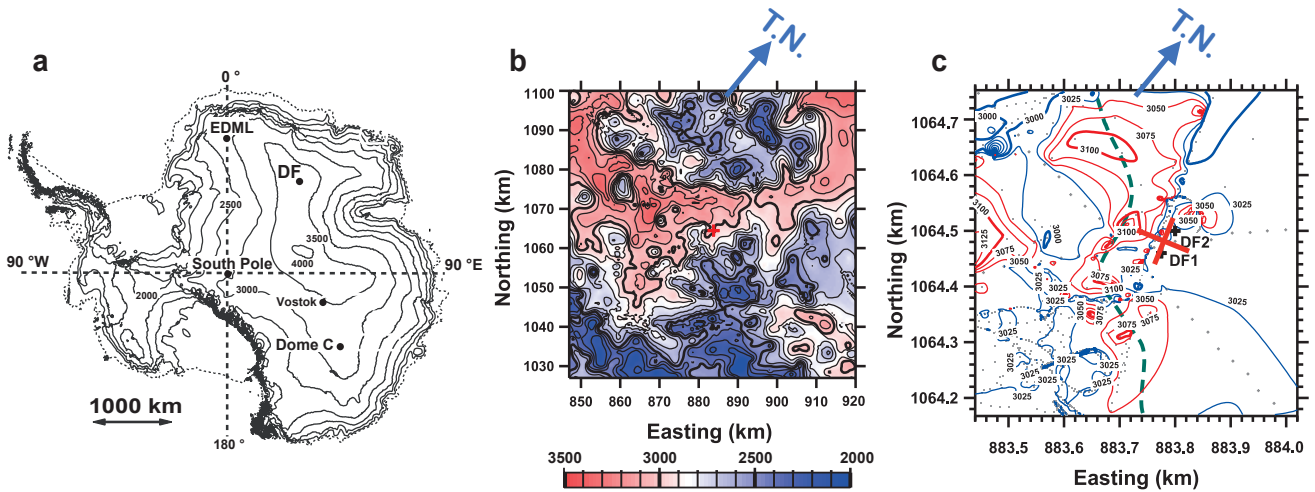
Figure 1. Maps of the coring site. (a) Surface elevation using a digital elevation model (Bamber et al., 2009). Maps showing ice thickness over areas of (b) 72 km^2 and (c) 580 m^2. In (b) and (c) the small red/black crosses near the centre of each map indicate the coring site. T.N. indicates true north. In (c) ice thickness is indicated by dots representing data from Tsutaki et al. (2022) and by markers representing data from Eisen et al. (2020). Thin and tThick areas are shown in red and blue, respectively, and the boundary is set at a thickness of 3000 m. The bold green dashed line indicates the presence of the local trough. The DF coring sites were located at the bank of this local trough, aligning with the estimated drainage routes of subglacial water (as shown in Figure 8d in Tsutaki et al., 2022). In (c), the two principal axes of the elongated single pole fabric inferred from polarimetric radar sounding (Fujita et al., 2006) are indicated as a large red cross.

2. 3. Methods and samples

As noted, this work utilized the DTM based on thick sections together with Laue X-ray diffraction method and microstructural observations using thin sections. The DTM provided data concerning the *c*-axis fabric in the form of eigenvalues with high sampling frequency, spatial resolution and continuity. However, this method does not produce information regarding the crystal axes of individual grains. Additionally, if a cluster of *c*-axes is significantly inclined from the vertical, it is impossible to derive correct eigenvalues without knowing both the angle of inclination and horizontal orientation of the *c*-axis cluster. In contrast, the Laue X-ray diffraction technique provides detailed information concerning both the *c*-axis and the *a*-axis of each crystal grain. Additionally, the use of an automatic fabric analyser (model G50, Russel–Head Instruments) allowed an assessment of variations in crystal orientation between grains. Using both the G50 analyser and microscopy, microstructural observations were performed as a means of assessing dynamic recrystallization and grain morphology. The methods described above provided a significant quantity of data concerning variations in crystalline texture along the ice core.

2.1 2. DF ice cores

The DF ice core was drilled on the Antarctic plateau (Figure 1) at a location with 77°19' S latitude and 39°42' E longitude that was 3810 m above sea level. The ice thickness is 3028 ± 15 m (DFICPM, 2017). The annual surface mass balance at this location has ranged from approximately 24 to 28 kg m^{-2} y^{-1} over the last 5000 years (Oyabu et al., 2023) and the annual mean surface air temperature is –54.4 °C (Yamanouchi et al., 2003). Deep ice cores have been drilled at DF on two occasions (e.g., Motoyama et al., 2020). The first core, DF1, was 2503 m in length and was drilled in the 1990s. The second,

DF2, had a length of 3035 m and was drilled between 2004 and 2007 in a borehole 44 m removed from the previous borehole (Figure 1c). The DF2 core specimen was employed in the present study. Both drilling sites are situated above a subglacial slope, positioned between bedrock high in the east and a subglacial trough with an ice thickness of approximately 3100 m in the west (Figures 1b and 1c). An ice thickness of approximately 2850 m marks the boundary between a thawed bed (in the case of thicker ice) and a frozen bed (in thinner ice) (Fujita et al., 2012). It is thought that spatially inhomogeneous basal melting has produced the localized inclination of layers within the ice sheet (DFICPM, 2017). The layered structures are inclined by less than approximately 5° at shallow depths whereas, in the deeper sections, the inclination reaches angles as high as 45° at a depth of 3000 m. Ohno et al. (2016) reported the distribution of air hydrates and isotopic composition of water in the deepest 1% (3000–3035 m) of the DF ice core. These factors were found to reflect the basic layered structure of the ice core except in the deepest few meters. However, this prior work did not investigate crystalline textural properties.

At present, DF is very close (within 10 km) to the dome summit and associated with a steep north-south surface mass balance gradient (Fujita et al., 2011; Tsutaki et al., 2022). This morphology implies that the DF summit has migrated along this gradient in the north-south direction during glacial and interglacial periods over which the accumulation rate changed dramatically (e.g., Parrenin et al., 2016). Thus, DF is subject to deviatoric stress in the direction of maximum inclination at each time. Azuma et al. (1999, 2000) reported that, in the case of the DF1 core, the *c*-axis fabric exhibited an elongated single pole fabric that was already observable at shallow depths. Fujita et al. (2006) investigated DF using polarimetric radar sounding and assessed the extent of radio wave birefringence caused by this elongated single pole fabric to depths of approximately 2200 m. Fujita's work demonstrated that the orientations of the elongated single pole fabric were, at least to this depth. Figure 1c presents the two principal axes assumed for the elongated *c*-axis fabric as a large red cross, aligning with the orientation of the subglacial slope (WNW) and its orthogonal direction.

2.2 ~~3.1~~ Dielectric Tensor Method

2.2.1 ~~3.1.1~~ Method

The principles of the open resonator method for determining the relative permittivity (ε) of thin samples have been previously described in the literature (Jones, 1976a, b; Cullen, 1983; Komiyama et al., 1991). The authors have since developed this technique to allow investigation of the tensorial permittivity of thick samples based on continuous radio birefringence scanning along an ice core (Matsuoka et al., 1998; Fujita et al., 2009, 2014, 2016; Saruya et al., 2022a, b; Inoue et al., 2024). The present work employed a microwave beam to study thick samples and ε values were obtained as volume-weighted averages within the volume encompassed by the Gaussian distribution of the beam. By setting the angle between the axis of the *c*-axis cluster and that of the electric field to approximately 45°, radio birefringence was generated as a result of the macroscopic permittivity of the crystals (e.g., Hargreaves 1978). Sweeping the radio wave frequency to detect resonances satisfying TEM $_{0,0,q}$ modes (where TEM is an acronym for transverse electromagnetic and q is an integer) allowed twin resonant peaks caused by dual permittivity components to be detected. These two components corresponded to ε along the axis of the *c*-axis cluster and along the orthogonal axis, representing components on the plane of the electric field vector (orthogonal to the axis of beam incidence).

2.2.2 ~~3.1.2~~ Open resonator and samples

This work employed two resonators (designated Nos. 1 and 2), the specifications of which are summarized in Table S1 in Supplementary Information Section 1.1. An open resonator employing frequencies between 26.5 and 40 GHz (entry 1 in Table S1) was utilized to assess the ice in the lowermost 20%. This resonator differed from that employed to study the ice above 2400 m, which operated at frequencies between 15 and 20 GHz (entry 2 in Table S1). These two resonators, each

having a semi-confocal shape with a flat mirror and a concave mirror, were designed to produce beam diameters of 16 and 38 mm, respectively (Figure 2). The consistency of the data obtained with the two resonators was confirmed by comparing the $\Delta\varepsilon$ values at depths between 2400 and 2500 m (Figure S1 in Supplementary Information Section 1.1). The smaller beam size of resonator No. 1 allowed the analysis of smaller samples (such as narrow quadrangular prisms) with higher spatial resolution. The No. 1 and No. 2 resonators were able to analyse ice specimens having thicknesses of at least 40 and 90 mm, respectively. The sizes of the samples examined in this work are summarized in Figure 2 and Table S2. Both the upper and lower surfaces of each specimen were microtomed to provide extremely smooth and precisely parallel surfaces. The DTM involved a series of measurements at 20 mm intervals along core segments having lengths of 0.5 m acquired at 2.5 m depth intervals. In the case of samples acquired below 2736 m, the core axis was rotated horizontally in the open resonator apparatus to ensure that the twin resonances could be detected. The experimental data were acquired at temperatures in the range of -30 ± 1.5 °C.

In addition to increases in the layer inclination, the axis of the c-axes cluster also exhibited an increased inclination such that this axis deviated from the vertical (hereinafter, referred to as the angle of inclination) in the same direction as the normal to the maximum layer slope. The relative orientation between each layer and the c-axes cluster was assessed by investigating the angle of inclination of the layer near the thin-sections used for the Laue X-ray diffraction method. These data confirmed that the horizontal direction for the c-axis cluster and the normal axis of each layer were within the approximately same vertical plane throughout the lowermost 20% of the DF ice core. Additionally, the horizontal orientation of the c-axes cluster varied with depth due to the rotation of the ice cores. In the case that both the angle of inclination and horizontal orientation of the c-axes cluster varied with depth, only the non-principal components of the permittivity tensor were determined within the ice using the DTM. Since the electromagnetic wave used in the DTM method has a transverse electric field, if the surface of the actual plate-shaped sample does not align with the principal axes of the crystal tensor, only the components in the misaligned orientation will be obtained. This misaligned orientation is referred as non-principal. Geometrical corrections to translate from the measured non-principal components to the principal components were applied using both the angle of inclination and horizontal orientation of the c-axes cluster as derived from c-axis fabric data acquired using a thin section method. The procedures used to perform these corrections are detailed in Supplementary Information Section 2. The non-principal components of the dielectric anisotropy ($\Delta\varepsilon'$) were also adjusted to align with the principal components ($\Delta\varepsilon$). It should also be noted that the DTM is a useful means of finding the $\Delta\varepsilon$ values of girdle-type ice fabrics. We can refer to the basic principles summarized in Supplementary Information Section 1.2.
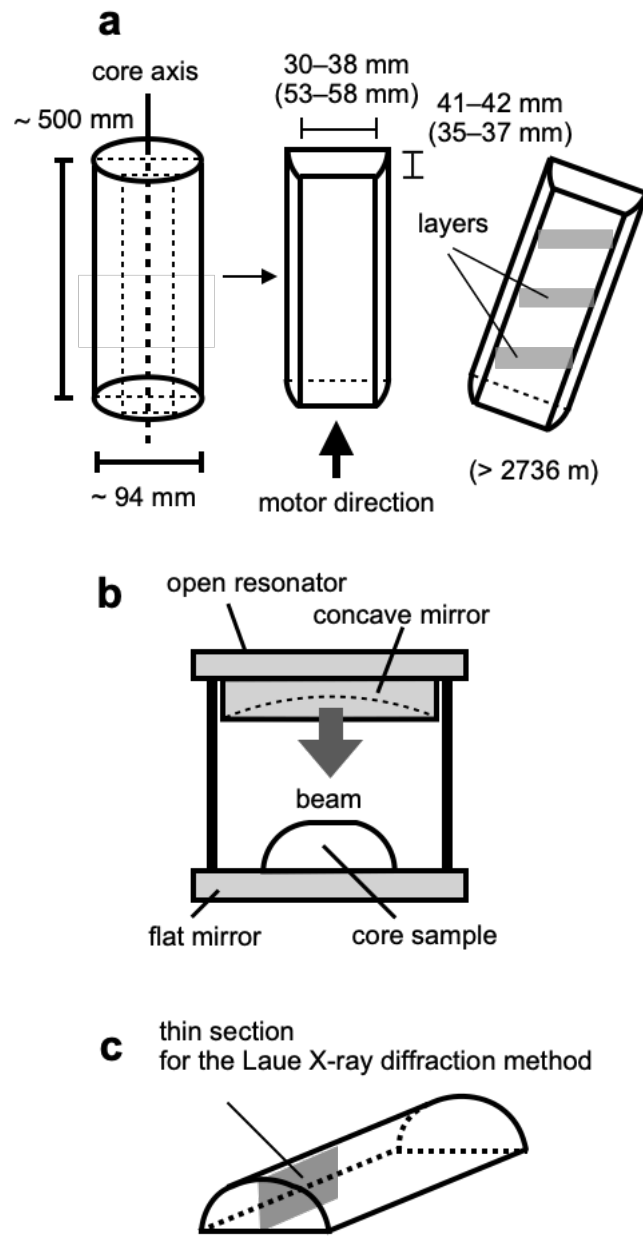
Figure 2. Diagrams of the (a) core cutting geometry and scanning direction, (b) the analytical setup as viewed from the front, and (c) the location of a thin section assessed using the Laue X-ray diffraction method.

2.3 3.2 Characterizations by Laue X-ray diffraction, microstructural observations and automatic fabric analyser

The Laue X-ray diffraction method was applied to thin sections measuring 100 × 45 mm (in the vertical and horizontal directions, respectively) and with thicknesses of less than 0.5 mm. This technique can determine the orientations of all axes of each crystal grain with an accuracy on the order of 0.5° (Miyamoto et al., 2011). A total of 42 depths within the lowermost 20% were selected for analysis and the Laue patterns were analysed after obtaining all the Laue figures. Here, the data for each thin section are expressed as the distribution of *c*-axes and *a*-axes on a Schmidt net diagram. The median inclinations of the *c*-axes with respect to the axis of the *c*-axes cluster were also calculated. The median inclination was defined as one half of the apex angle of the cone in which one half of the measured *c*-axes were included from the centre axis of the *c*-axes cluster.

Additionally, microstructure observations were carried out using both the G50 instrument and optical microscopy to investigate the manner in which microstructural evolution affected the development of the *c*-axis fabric and to assess fluctuations in the same thin section. These analyses were performed at several preselected depths. Thin sections were prepared from the vertical plane of the ice cores, measuring 90 mm in the depth direction and 50 mm in the horizontal

direction and with thicknesses of 0.5 mm. Images of the *c*-axis fabric were obtained using the G50 automatic fabric analyser to investigate the relationship between the morphology and *c*-axis orientation of each grain. The grain numbers included in the Gaussian beam or thin section are provided in Table S3.

2.4 3.3 Grain size and layer inclination measurements

The grain sizes at the DF site were ascertained in this work based on visual observations of faint differences in light reflectivity between grains and visible grain boundaries. While freshly cut surfaces did not exhibit these features, the ice cores in storage developed these reflectivity variations over time as sublimation progressed. The average surface area of each grain was determined using three circular gauges with diameters of 10, 20 and 40 mm and by counting the number of grains on the core surface within the circle of the gauge. The number of crystal grains within each circle typically ranged from several to 20, with an estimated error as high as 20% of the crystal quantity. These examinations were performed at 1.5 m intervals to a depth of 2967.5 m. Below this depth, the crystals were much larger and it became difficult to define the grain sizes. Changes in the angles of inclination of visible features (such as cloudy bands or tephra layers) relative to the horizontal were also investigated using a protractor. This process is explained in detail in Supplementary Information Section 1.3. It should also be noted that this method did not take into account core rotation resulting from core breaks. The present work provides detailed data supplementing that in a preliminary report (DFICPM, 2017).

3. 4. Results

3.1 4.1 Depth-dependent variations in measured $\Delta\varepsilon'$, corrected $\Delta\varepsilon$ and standard deviation values

The $\Delta\varepsilon'$ data are presented in Figure 3 while examples showing the continuous variation of $\Delta\varepsilon'$ along a core segment having a length of 0.5 m are provided in Supplementary Information Section 3. Here, the symbols and error bars indicate the mean values and the standard deviations (SDs) determined at 0.5 m intervals along the core sample while the dots represent raw data. Black and red symbols indicate data obtained without and with inclined measurements, respectively. Data acquired without and with the horizontal samples inclined within the resonator are in agreement over the depth range of 2630–2730 m for which both measurements were performed. This outcome confirms that horizontal rotation of the samples in the open resonator did not affect the experimental relative permittivity values. Note that, overall, the $\Delta\varepsilon'$ values exhibit a decrease with increasing depth and the data show more scatter at greater depths. Below 2900 m, the $\Delta\varepsilon'$ values largely fluctuated.
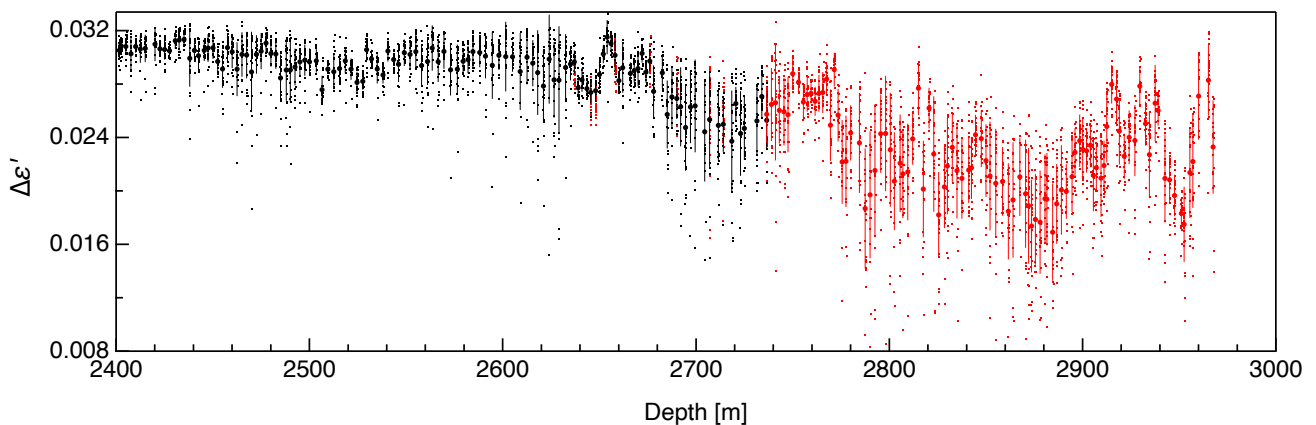
Figure 3. The $\Delta\varepsilon'$ data generated in this work. Dots represent raw data acquired at 0.02 m intervals. Symbols and error bars indicate the mean values and SDs for each 0.5 m interval. Black and red indicate data obtained without and with rotation of the samples in the open resonator, respectively (see Figure 2).

3.2 4.2 The *c*- and *a*-axis orientations determined using the Laue X-ray diffraction method

The c- and a-axis distribution data obtained from the Laue X-ray diffraction are given in Figure 4. The c–axis fabric was found to generally exhibit a significant single-pole cluster, the strength of which fluctuated with increasing depth. Because each grain in the hexagonal crystal lattice had three equivalent a-axes orthogonal to the c-axis, the distribution of the a-axes formed a girdle plane orthogonal to the c-axes cluster at each depth. Figures 4(m–q) display data from the deepest five depths, all of which were within the bottom 2% of the ice sheet. In these figures, the red and blue numerical markers indicate the distributions of the c-axis and a-axis, respectively, at each depth. As a consequence of grain growth near the bed of the ice sheet, no more than six crystal grains were found in a thin section and the centre of the clusters could not be determined with this very limited number of grains. With the exception of these five depths, both the angle of inclination and the horizontal orientation of the c-axes cluster could be ascertained based on analysis of the c-axis fabric, as shown by Views 1 to 3. Both these factors were subsequently used to correct $\Delta\varepsilon'$ values to $\Delta\varepsilon$ data and the procedure used for these corrections is detailed in Supplementary Information Section 2. The median inclination of the c-axes cluster values was also calculated using c-axis fabric data acquired from thin sections. Both the angle of inclination from the vertical and median inclination values for the c-axes cluster are presented in Figure 5f. The angle of inclination of the c-axes cluster was found to increase monotonically at greater depths down to 2967 m.

The a-axis fabric generally exhibited pronounced girdle-type clustering on each plane. Similar to the c-axis cluster data, the strength of this girdle clustering effect varied with increasing depth. Because each grain had three equivalent a-axes orthogonal to the c-axis, the distribution of the a-axes in a girdle plane typically displayed maxima at 60° intervals. The depth profiles in View 4 indicate that the normalized density, ρ, of the a-axis along the girdle plane of the a-axis exhibits a variable relationship with θ. In some cases, there are significant variations at 60° intervals, as can be seen in Figures 4b, 4e and 4g.

The c-axes distribution of each thin section and the a-axes inhomogeneity are also presented in Figures 5c and 5d. Crystal grains having a c-axis orientation in the range of 30°–60° were found at depths below 2600 m, with the exception of the impurity-rich layer indicated by brown shading. Here the term impurity-rich means that the ice contains either insoluble particles (like dust) and/or soluble impurities such as dissolved ionic species. The a-axes inhomogeneity was defined as the SD of the a-axes density, ρ, (hereinafter, SD_ρ) as shown in View 4 in Figure 4. Here, larger values correspond to more anisotropic a-axes distributions. The data demonstrate relatively small and large extents of inhomogeneity in the impurity-rich and impurity-poor layers, respectively, and show that the SD_ρ of the a-axis inhomogeneity undergoes large fluctuations associated with transitions between glacial and interglacial periods. It is also very important to note that the SD_ρ data appear correlated with the grain size (Figure 5e).

251
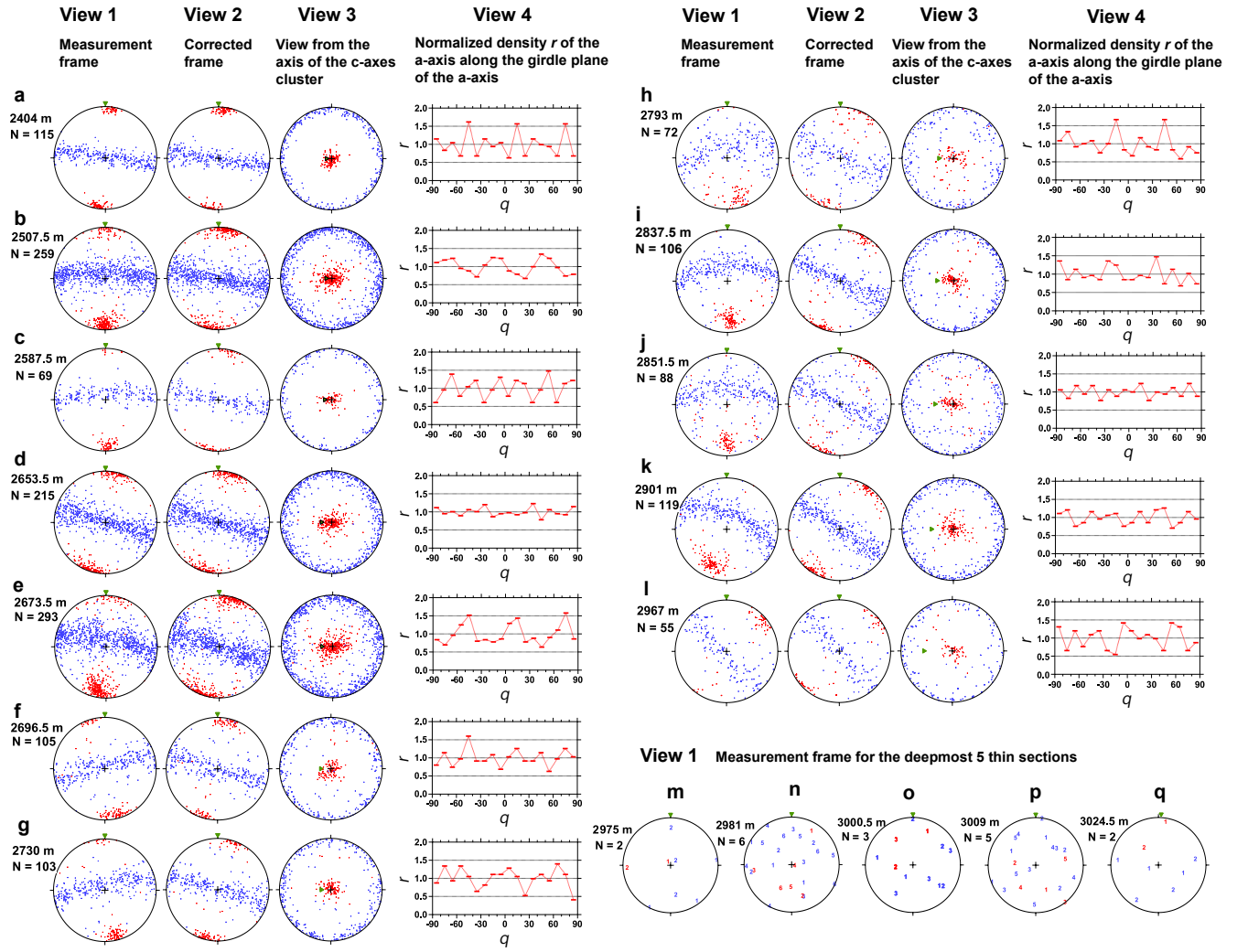
Figure 4. The *c*-axis and *a*-axis distribution data obtained from the Laue X-ray diffraction analyses using 17 depths out of a total of 42. (a) to (l) present data for the 12 shallower depths over the range of 2400 and 2967 m in the form of three equal area Schmidt net diagrams (e.g., Langway, 1958). These diagrams summarize the projected *c*-axis and *a*-axis distributions as indicated by red and blue symbols/markers, respectively. For these 12 depths, the leftmost diagrams (View 1) show projections from the measurement frame (refer to Figure S2b) while the second series of diagrams (View 2) is a projection from the corrected frame (see Figure S2b'). The third series of diagram (View 3) is a projection from the centre of the *c*-axes cluster. The green triangle in each diagram indicates the vertical orientation in the ice sheet, which approximately aligns with the core axis (though the borehole inclined 3–6° from the vertical) The fourth column contains plots of the normalized density, ρ, of the *a*-axis along the girdle plane of the *a*-axis against θ (in degrees), which is the angle from the top of the figure in View 3. The figures in (m) to (q) show projections from the measurement frame for the deepest five depths, ranging from 2975 to 3024.5 m. Because of grain growth near the bed of the ice sheet, each thin section contained less than six grains. Rather than dots, numerical markers are used to indicate the orientation of each grain.

3.3 ~~4.3~~ Depth-dependent variations of corrected Δε and SD values and eigenvalues

In this work, $\Delta\varepsilon'$ values were corrected to $\Delta\varepsilon$ data using both the angle of inclination and the horizontal orientation of the *c*-axes cluster as estimated from the Laue X-ray diffraction method. The correction procedure is described in Supplementary Information Section 2. Figure 5a plots the corrected $\Delta\varepsilon$ values and eigenvalues obtained using the Laue X-ray diffraction process. As was also the case in Figure 3, the symbols and bars here indicate the mean values and the SDs determined at 0.5 m intervals along the core sample. Assuming a single-pole fabric without horizontal anisotropy, the relationship between the $\Delta\varepsilon$ and eigenvalue data can be expressed as $a_3^{(2)} = (2\Delta\varepsilon / \Delta\varepsilon_s + 1) / 3$, where $\Delta\varepsilon_s$ is the dielectric anisotropy of a single crystal. The $\Delta\varepsilon$ values (Figures 5a) reached a maximum of approximately 0.031 at depths of 2430 and 2654 m and then proceeded to exhibit significant fluctuation. The evident decrease in $\Delta\varepsilon$ values and increase in the SDs are a direct consequence of the

272   scatter in the individual $\Delta\varepsilon$ measurements (represented by the dots in Figure 5a). In the case that this is pronounced, the

273   mean $\Delta\varepsilon$ value for a 0.5 m segment becomes smaller and the SD larger. At depths greater than approximately 2900 m, the $\Delta\varepsilon$

274   values exhibit greater fluctuations over distances on the order of 10 m. It should also be noted that the $\Delta\varepsilon$ for each ice core

275   specimen show large negative spikes in conjunction with large SDs, as demonstrated by the dots in the panel and the typical

276   profile presented in Figure S9.
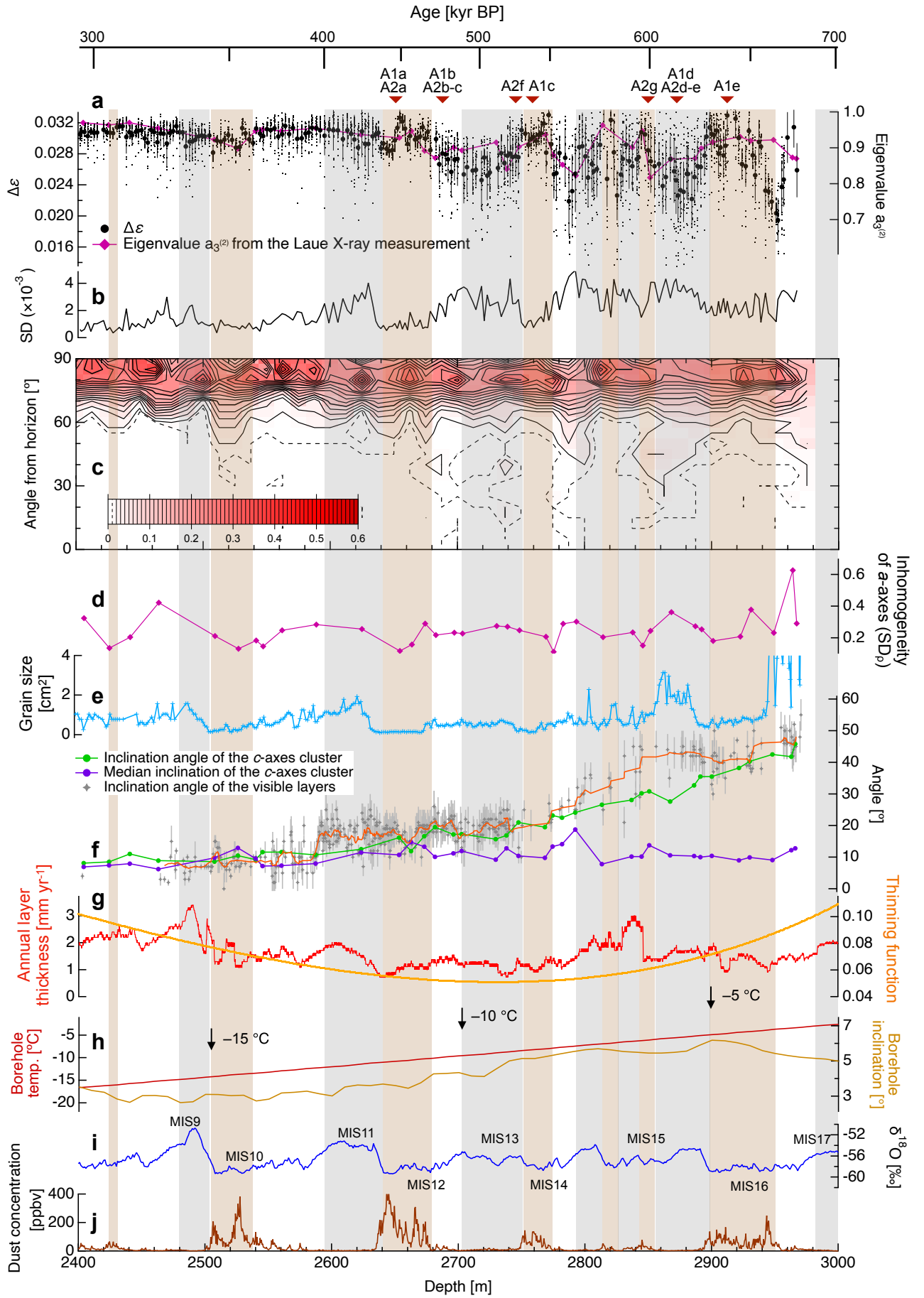
Figure 5. A detailed comparison of Δε values with various ice core data. (a) Δε (mean and raw data generated using the DTM) and eigenvalues (from the Laue X-ray diffraction method). The potential uncertainty in the eigenvalues based on the total number of grains

sampled is discussed in Supplementary Information Section 1.4. (b) SD values. (c) The distribution of *c*-axes angles relative to a plane orthogonal to the *c*-axes cluster as generated using data obtained from the Laue X-ray diffraction method. The probability of the presence of *c*-axes in a given region is shown by the contour lines. (d) The inhomogeneity of the *a*-axes as demonstrated by the SD of the *a*-axes density, ρ (SD$_\rho$). (e) Grain size data. (f) The angles of inclination of the *c*-axes cluster and the layers determined by visual observations together with median inclinations. The orange line was generated by smoothing of the angle of layers at ten measuring points. (g) Data showing annual variations in the layer thickness and thinning function (DFICPM, 2017). (h) Borehole temperature and inclination data (Motoyama et al., 2020). (i) δ^{18}O data (DFICPM, 2017). (j) Concentrations of dust particles (DFICPM, 2017). Gray and brown shading indicate interglacial periods and depths having higher concentrations of impurities (that is, impurity-rich layers), respectively. The depths at which microstructures were observed are indicated in the upper part of the figure.

3.4 4.4 Grain sizes, layer inclinations and microstructures

The grain size and angle of inclination data for the visible layers are presented in Figures 5e and 5f, respectively. The grain sizes associated with interglacial and glacial periods were found to be significantly larger and smaller, respectively, with this difference becoming more pronounced at greater depths. It is also apparent that the $\Delta\varepsilon$, the SD values for the $\Delta\varepsilon$ data, and the grain sizes were approximately synchronous, implying the presence of a common underlying factor. The grain sizes exhibited no overall increase trend with increasing depth. The grain sizes at depths between 2900 and 2950 m remained small despite temperatures higher than -5 °C in this region. However, at depths greater than 2960 m (equivalent to the deepest approximately 2% of the core), the grain sizes were extremely large, often reaching sizes in excess of 300 cm^2. The sizes can be seen to have fluctuated and there is a clear distinction between the very small grains in the impurity-rich layers and the larger grains in the impurity-poor layers. The grain size data acquired below 2950 m are shown in Figure 6.

The inclination angle of the visual layers (see orange line in Figure 5f) shows stepwise changes at 2580 and 2770 m, being 10° at depths less than 2580 m, 20° at 2770 m, and reaching 45° at 3000 m. The present data demonstrated that the angles of inclination of the *c*-axes cluster and of the visual layers deviated over a wide range of depths below approximately 2580 m (Figure 5f). This deviation was most pronounced at depths between 2800 and 2900 m.

Results and discussions of microstructures are given in Appendix A. Microstructural observations demonstrated the different manner concerning dynamic recrystallization and the crystal morphology between the impurity-rich and impurity-poor layers (see Appendices A1, A2, and Figure A1). Evidence of migration recrystallization, such as bulged grain boundaries and interlocking grains, as well as potentially nucleated grains, were found in impurity-poor layers (see Appendix 3 and Figure A2).
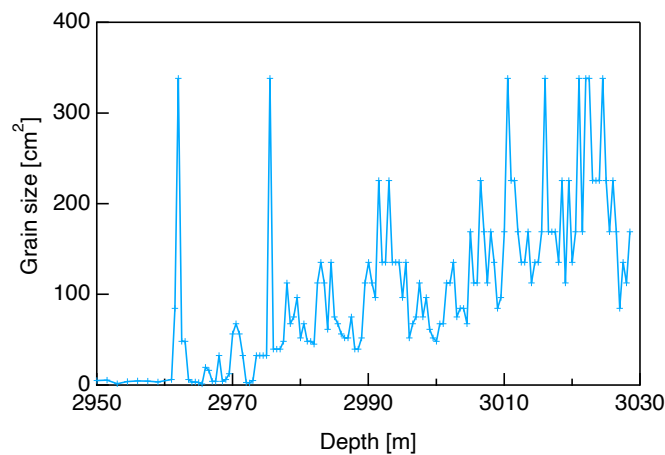
Figure 6. Grain size data acquired below 2950 m. Note that the scale of the vertical axis is significantly different from that in Figure 5e.

4. 5. Discussion

4.1 ~~5.1~~ Development of crystal orientation fabric and layered structures in the deep sections: common and unique features of the site

The relationships between $\Delta\varepsilon$ values and normalized eigenvalues, $a_3^{(2)}$ and grain sizes in the DF and EDC ice cores were examined (Figure 7). These two sites are similar in terms of glaciological conditions, including surface temperature, annual mean surface mass balance and ice thickness (EPICA Community Members, 2004; DFICPM, 2017). In addition, the dust flux profiles of the DF and EDC ice cores are very similar (DFICPM, 2017). The general trends exhibited by cluster strength and grain size were found to be close to equivalent in both ice cores. Surprisingly, the c-axes cluster strength in the DF ice core was almost the same as that in the EDC ice core, even though the layer structures in the DF were largely inclined. Hence, layer inclination appears not to affect cluster strength. Durand et al. (2009) pointed out similar depth-dependent developments in c-axis clustering in deep sections of the GRIP ice core in Greenland (Thorsteinsson et al., 1997) and the EDC core in Antarctica. The equivalency among these three sites across both hemispheres implies that certain physical mechanisms are driving this similar development of c-axis clustering. The authors propose that the ambient temperature within these ice sheets could have produced this effect through mechanisms such as dislocation creep and recrystallization. At a depth of approximately 2400 m, the thickness of the ice was close to 10% of the original ice equivalent thickness at the time of deposition (see Figure 5g), with an eigenvalue, $a_3^{(2)}$, of approximately 0.93. A highly clustered texture is unlikely to form in the case of zero or minimal shear stress as a means of compression or shear, such that dynamic recrystallization occurs as an accommodation process. This state of saturation of the c-axis cluster, along with the common temperature range may be more effective triggers for nucleation and recrystallization. The deepest 10–20% of the polar ice sheets is typically characterized by ready deformation in response to horizontal shear because of the presence of high temperatures and a highly clustered c-axis fabric. At these depths, dynamic recrystallization plays a critical role, particularly in impurity-poor layers, in the recovery of various c-axis orientations capable of promoting deformation based on dislocation creep.

A unique feature of the DF ice core is the inclined layered structures. The coring site is situated on a bank very close to a subglacial trench (Figure 1c), with both the depth difference and distance between the two being approximately 100 m. This geometry corresponds to the maximum angle of inclination of the c-axes cluster of approximately 45° and the angle of inclination of the visually-identifiable layers of approximately 45° near the base of the ice sheet (Figure 5f). This deeper trench may act as a pathway for the flow of subglacial water while the deeper bed can accumulate meltwater (e.g., Pattyn, 2010, Fujita et al., 2012). Thus, the authors suggest that a simple shear strain component is directed towards the subglacial trench. The rheology of polycrystalline ice with a single-pole fabric is similar to that of single crystal ice, in that both will readily deform in response to simple shear stress. In the case of DF, because of the friction force between ice and inclined bedrock, simple shear system would rotate the entire system including the internal layers and the c-axes cluster together. In principle, simple shear is a superposition of pure shear and the rigid-body rotation of the system, and layer inclination is a result of the latter rotation. The c-axes also are included within the system's rigid-body rotation. However, normal components of the strain (both compression in the near-vertical and extension near the horizontal plane) causes the rotation of c-axes cluster alone toward the vertical by intracrystalline slip at the same time. In this way, total amount of inclination becomes larger for the layers than the c-axes cluster. Thus, the mismatch between the angles implies that simple shear was the primary mechanism within this depth range. Considering the consistency of the eigenvalues between the DF and the EDC ice cores (Figure 7), the rigid-body rotation appears not to affect cluster strength. The nature of deep sections in the DF ice core is similar to that of the EDML ice core (Weikusat et al., 2017), which is located in a divide region where horizontal flow occurs. In the deepest sections of the EDML ice core, strong shear stress parallel to the bedrock is predominant. In contrast, the DF ice is located within a dome region. Even in the case that vertical compression is predominant in shallow sections, shear stress may be the primary mechanism in deeper sections due to the bedrock inclination.

352
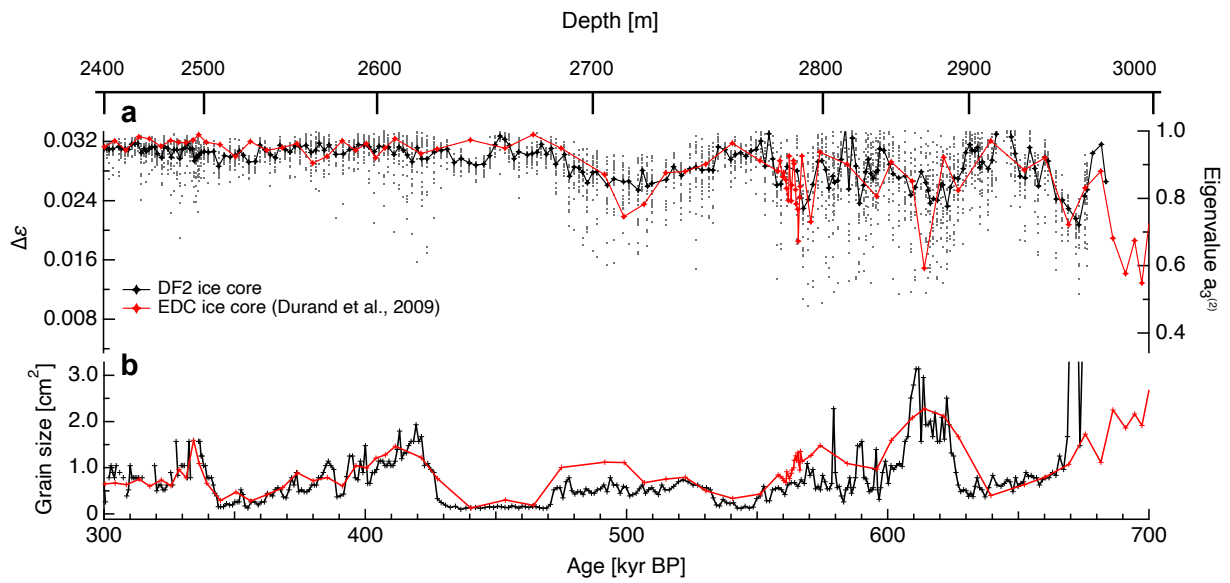
Figure 7. A comparison of the *c*-axis fabric and grain size data obtained from the DF core and the EDC core, applying the AICC2012 age scale (Bazin et al., 2013). (a) $\Delta\varepsilon$ presented as raw data (dots) and as mean values for 0.5 m segments (black symbols for DF data) or for each thin section (red symbols for EDC data). The right hand axis provides a scale for normalized eigenvalues. (b) Grain sizes in the DF and EDC cores. The EDC data are from Durand et al., 2009.

4.2 ~~5.2~~ Large-scale development in the crystal orientation fabric and grain sizes: variations during the glacial/interglacial periods

A clear advantage of DTM is that data with high sampling, spatial resolution and continuity allowed for the evaluation of *c*-axes cluster fluctuations in comparison with various ice core data. Saruya et al. (2022b) investigated the factors affecting the *c*-axis fabric at depths above 2400 m by assessing correlations between $\Delta\varepsilon$ and various ionic impurities and dust concentrations. They found that $\Delta\varepsilon$ exhibited a positive correlation with the concentration of Cl^- ions but an inverse correlation with the amount of dust particles. In contrast to depths above 2400 m, the relationship between $\Delta\varepsilon$ and Cl^- ions was unclear below 2400 m. This work compared $\Delta\varepsilon$ with grain size, $\delta^{18}O$ and dust particle concentration (Figure 5a, 5e, 5i and 5j). It is well known that glacial ice includes many soluble impurities as well as dust particles (i.e., impurity-rich ice). Referring to the $\delta^{18}O$ profile, it is apparent that the mean $\Delta\varepsilon$ values decreased (caused by the large scatter of data points) during interglacial periods at depths below 2640 m. These decreases became more pronounced as the scatter of the raw data became more significant at greater depths. The SDs were smaller in samples associated with glacial periods and larger during interglacial periods (Figure 5b). High concentrations of impurities had an apparent effect on the $\Delta\varepsilon$ values, maintaining consistently high $\Delta\varepsilon$ below 2600 m (Figure 5a). Small grain sizes were also present (Figure 5e). Overall, the grain sizes together with the *c*-axis fabric were found to be interdependent and strongly correlated with the presence of impurities.

Above 2400 m, the grain size grew steadily (but with a partial decrease during the two glacial periods) (Azuma et al., 1999, 2000). However, below 2400 m, there was no overall increase in grain size. During interglacial periods, the grain size gradually increased with depth but decreased sharply during glacial periods that were associated with higher impurity concentrations. At the lower glacial ice boundary, the grain size again became smaller, indicating that grain size growth was interrupted during glacial periods. This pattern has also been reported to occur in the EDC core (Durand et al., 2009). The reason why grain growth in deeper ice is interrupted during glacial periods remains unclear, although this effect may be due to nucleation or migration recrystallization. Figures 5c and A2 show signs of nucleation and migration recrystallization (e.g., the presence of crystal grains having a *c*-axis orientation in the range of 30°–60° and bulging (cuspidate) grain boundaries), both of which can reduce the mean grain size, in interglacial ice specimens. These phenomena may suppress normal grain

growth and lead to smaller grain sizes. Furthermore, extremely large grains exceeding 10 cm in radius (~300 cm^2) were observed below 2960 m (Figure 6). Grains of this size have not been found in the EDC core to date (see Figure 7). Interestingly, small grains (less than 1 cm^2) were maintained at a depth of approximately 2900 m (MIS16), despite the high temperatures at that depth that were close to the melting point of ice (–5 °C). Although the concentration of dust particles was not so high in this region (less than 100 ppbv), the grain boundary pinning effect caused by dust particles remained still effective even at high temperatures.

Significant changes in the cluster strength and the distributions of c-axes angles were found below the impurity-rich layer at depths between 2640 and 2680 m. The fluctuations in $\Delta\varepsilon$ values increased significantly and the crystal grains having a c-axis orientation in the range of 30°–60° appeared. The reason for these changes remains uncertain, but one possible explanation is the activation of migration recrystallization. Migration recrystallization is thought to occur at temperatures higher than –10 °C. (e.g., Duval and Castelnau, 1995; Montagnat et al., 2009). The ambient temperature at this layer is approximately –10 °C. The authors propose that the activation of migration recrystallization caused these changes, and the dusty impurities that influence the grain boundary mobility are responsible for the degree of this process.

4.3 ~~5.3~~ Impacts of dust particles and dynamic recrystallization on the crystal orientation fabric and grain sizes

The behaviour of dynamic recrystallization highly depends on the temperature and impurities (e.g., Humphreys and Haterly 2004; Cuffey and Paterson, 2010). It should be also noted that the relationship between cluster strength and the concentration of dusty impurities changes at approximately 2640 m. Impurity-rich layers maintained a high degree of clustering whereas layers having fewer impurities showed relaxation. According to a case study concerning the NEEM ice core by Eichler et al. (2017) and a review by Stoll et al. (2021b), dust particles are located not only at grain boundaries but also in grain interiors and at triple junctions. It is well known that dust particles restrict grain growth and result in smaller grain sizes (e.g., Alley and Woods, 1996). This trend was observed in the present study. The scatter plot of the $\Delta\varepsilon$ values, grain sizes and concentration of dust particles are given in Figure 8. The grain sizes are decreased as the concentration of dust particles increased (Figure 8b). However, the role of dust particles in ice deformation via dislocation creep is not well understood. Dust particles can produce ~~product~~ dislocation or may act as sink of dislocations similar to grain boundaries. Saruya et al. (2022b) suggested two possible actions of particles: (i) restricted deformation due to the inhibition of dislocation by dust particles and/or (ii) the promotion of diffusion creep that does not cause c-axis rotation. Diffusion creep is known to be promoted by smaller grain sizes. Which of these effects is more dominant is not currently known although either one could restrict c-axis clustering. The present work found that the degree of c-axis clustering in impurity-rich layers containing dust below 2640 m was stronger than that in the surrounding layers. Below 2640 m, the $\Delta\varepsilon$ values were found to be increased with as the concentration of dust particles increased (Figure 8a). This trend cannot be explained by the above two possibilities. Additionally, the consistently smaller grain sizes in the impurity-rich layers indicate that grain boundary migration was also restricted in such ice. This confirms that the movement of dislocations as line defects and of grain boundaries as planar defects within the crystal lattice was greatly affected by the presence of dust particles that act as obstacles.

The c-axis fabric contains information concerning the deformational history of the ice as well as grain growth and recrystallization (e.g., Cuffey and Paterson, 2010; Faria et al., 2014a, b). Ultimately, all these factors are sensitive to the deposition of insoluble impurities that limit grain boundary migration through Zener pinning mechanisms and also impede dislocation movement (Alley and Woods, 1996; Durand et al., 2006). The distribution of c-axes shown in Figure 5c indicates that crystal grains having a c-axis orientation in the range of 30°–60° appeared at depths below 2600 m. New grains are thought to have been formed with an orientation that promoted basal glide (e.g., Alley, 1992; Humphreys and Hatherly, 2004, Cuffey and Paterson, 2010), meaning approximately 45° from the compressional axis. Additionally, crystal grains having c-axis orientations in the range of 30°–60° were more frequent in the impurity-poor zones, in which the grain size was larger

and the $\Delta\varepsilon$ values lower. The authors propose that these grains with a c-axis orientation of 30°–60° correspond to nucleated grains in the deeper part of the ice and could have grown while eliminating older grains by migration recrystallization. These ice crystals would be expected to develop c-axis orientations that favoured dislocation-creep-based deformation. The formation of such grains as a result of nucleation is consistent with the observations of the corresponding grains (see Appendix A3 and Figure A2).

Concerning the a-axes organization, in the case that the degree of inhomogeneity of the a-axis within the girdle was expressed as SD_ρ, these values were generally larger in impurity-poor layers and smaller in impurity-rich layers (Figure 5d). Thirdly, the The SD_ρ values and grain size were approximately synchronous (Figures 5e). During dislocation creep, if the basal plane is the primary slip plane (that is, the easy-glide plane of hexagonal ice), it is unlikely that a-axis organization will occur geometrically on this basis. Since dislocation creep and a-axis organization do not seem interdependent, we can exclude this possibility. The organization of the a-axis structure among the crystal grains can occur as a result of interactions at the boundaries between adjacent grains. Therefore, the authors speculate that dynamic recrystallization processes, particularly migration recrystallization associated with nucleation, play a critical role.

The authors propose that grain nucleation and migration recrystallization lead to significant changes in the crystal orientation fabric. The decrease in $\Delta\varepsilon$ values and less clustered c-axis fabric in impurity-poor layers can be explained by the growth of grains having different c-axis orientations. Conversely, such grains were much smaller and limited in volume in the impurity-rich layers. Grain coarsening by migration recrystallization does not appear to occur because insoluble impurities restrict grain boundary migration (e.g., Durand et al., 2006; Stoll et al., 2021b) and so limit the growth of nucleated grains. Therefore, the change in the c-axis fabric (meaning a decrease in $\Delta\varepsilon$ values) caused by nucleation and migration recrystallization should be significant only in impurity-poor layers. On this basis, dynamic recrystallization would be expected to greatly affect the c-axis fabric development. Even in the case that grain nucleation occurs in both impurity-rich and impurity-poor ice, the contribution of this process to changes in the c-axis fabric would depend on the surrounding conditions. Hence, this effect may not be immediately apparent in terms of the volume-weighted mean $\Delta\varepsilon$ values obtained using the DTM. However, the growth of these nucleated grains, which occurs primarily in impurity-poor ice, and the subsequent strain-induced migration recrystallization could significantly affect the $\Delta\varepsilon$ values because of the growth of grains having different c-axis orientations. The influence of the migration recrystallization on the crystal orientation fabric at the deep sections in ice sheets has been also mentioned in the GRIP and EDC ice cores (Thorsteinsson et al., 1997; De La Chapelle et al. 1998; Durand et al., 2009), but the specific processes and contributions (such as differences in recrystallization activity between impurity-rich and impurity-poor layers, appearance of crystal grains having a c-axis orientation that was significantly offset from the surrounding grains, the mechanisms behind the relaxation and large fluctuations of c-axis clustering observed in the interglacial periods) were clarified in this work.
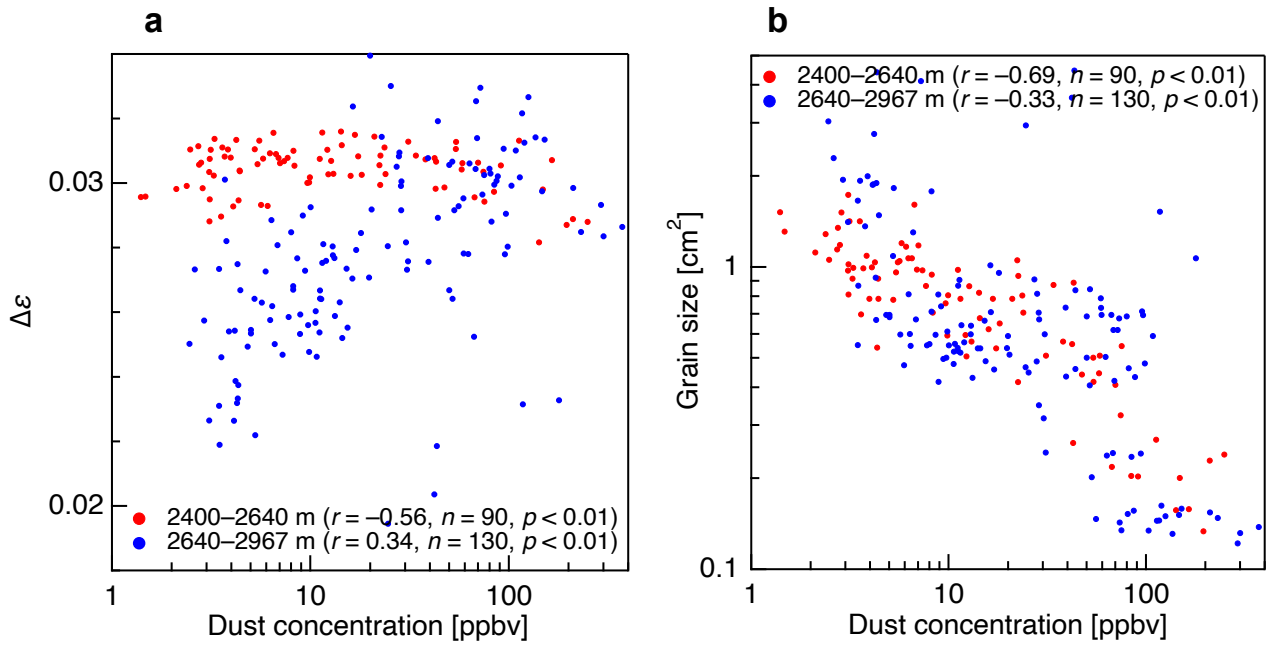
Figure 8. Scatter plot of (a) the $\Delta\varepsilon$ values and dust concentration and (b) grain sizes and dust concentration. Note that, in these figures, grain sizes and dust concentration are shown using logarithmic scales. In each panel, red and blue markers correspond to the data from 2400 to 2640 m and from 2640 to 2967 m depths, respectively. The correlation coefficient (r), sample number (n) and p-value (p) are given with the legend.

4.4 ~~5.4~~ Small-scale development of crystal orientation fabric and grain sizes: fluctuations within impurity-rich and impurity-poor layers

Closeup profiles and scatter plot for $\Delta\varepsilon$ values, grain sizes and concentration of dust particles at depths between 2600 and 2820 m are given in Figure 9. The $\Delta\varepsilon$ values exhibit a negative correlation with dust particle concentration in impurity-rich layers ($r = -0.55$ at depths between 2635 and 2676 m) but a positive correlation in impurity-poor layers ($r = 0.47$ at depths between 2678 and 2748 m) (Figure 9d). A similar negative correlation has been also observed at depths above 2400 m (Saruya et al., 2022b), suggesting that the variation in $\Delta\varepsilon$ values within impurity-rich layers originated at shallow depths and was preserved until deep sections. In contrast, the variation of $\Delta\varepsilon$ values within impurity-poor layers appear to develop at greater depths due to the migration recrystallization. The authors propose that the lower concentration of dust particles enhance migration recrystallization, leading to smaller $\Delta\varepsilon$ values. This suggests that, at greater depths, the deformation history in the impurity-rich layers is preserved, whereas that in the impurity-poor layers is updated (i.e., lost) by the active migration recrystallization. Additionally, as shown in a positive correlation in impurity-poor layers, even small amounts of dust particles and small variations in their concentration can significantly influence the crystal orientation fabric.

Another feature of the impurity-rich layers was consistently small grain sizes (see depths between 2635 and 2676 m, Figure 9b), an effect otherwise referred to as steady state grain size (e.g., Steinbach et al., 2017). This effect is thought to occur in the case that normal grain growth counteracts rotation recrystallization regardless of the initial grain size (Jacka and Li, 1994). The authors propose that the steady grain sizes in the impurity-rich layers appeared at greater depths. At shallower depths, the grain sizes would have been inversely correlated with the dust concentration.

478
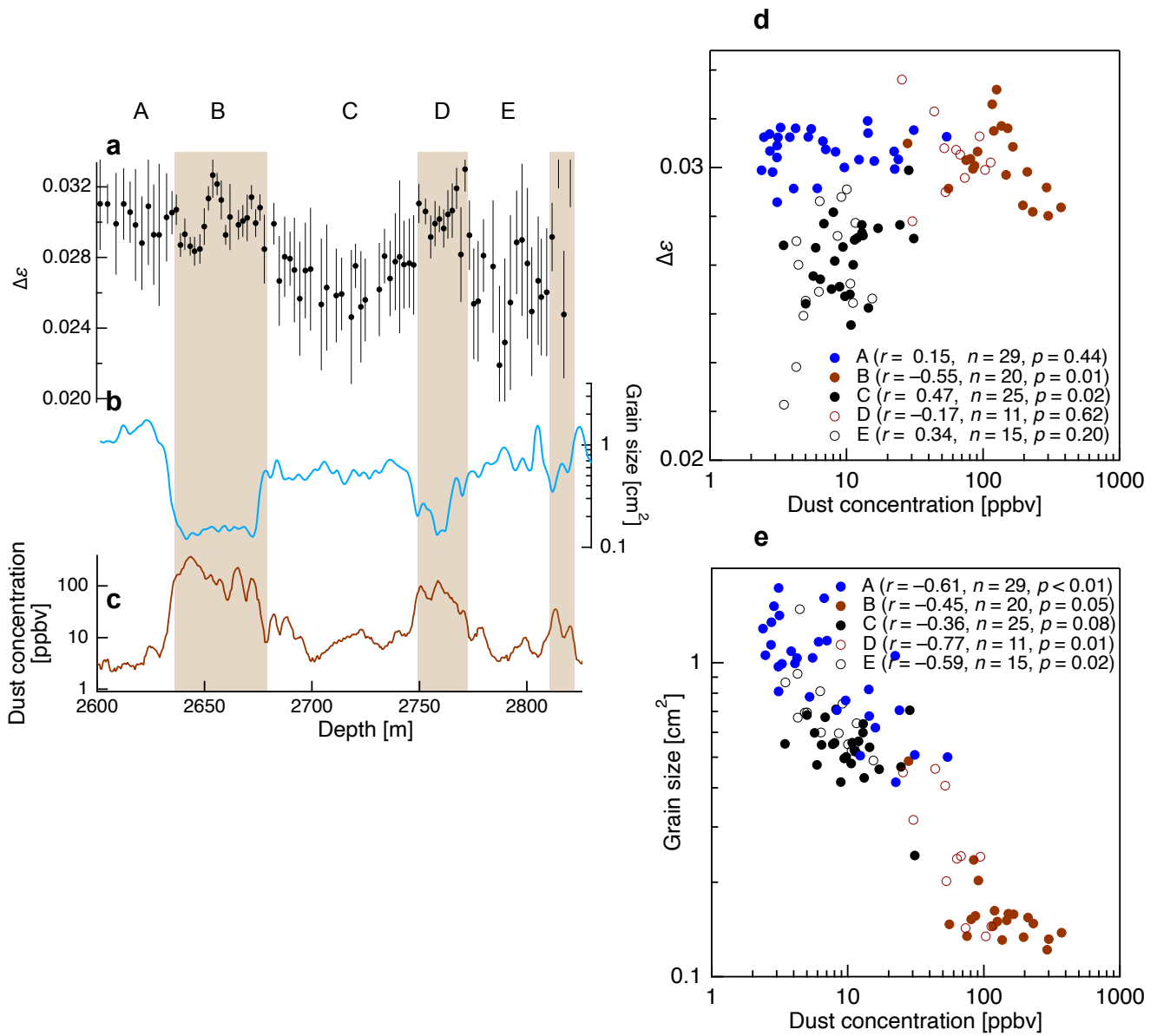
Figure 9. Detailed comparison of the $\Delta\varepsilon$ values, grain sizes and dust concentration at depths between 2600 and 2820 m. (a) to (c) present closeup profiles. Note that, in these figures, grain sizes and dust concentration are shown using logarithmic scales. Grain sizes and dust concentration profiles are smoothed over 2.5 m (grain sizes data were smoothed after interpolating to generate 0.5 m interval data). Brown shading (zone B and D) indicates impurity-rich layers. The boundary concentration of dust particles between impurity-rich and impurity-poor layers was approximately 30 ppbv. (d) Scatter plot of the $\Delta\varepsilon$ values and dust concentration (e) Scatter plot of the grain sizes and dust concentration. The correlation coefficient (r), sample number (n) and p-value (p) are given with the legend in the panels (d) and (e). A to E correspond to the depth zone given in the left panel. ~~Here B and D are impurity-rich layers.~~

5 ~~6~~ Conclusions

    With the aim of obtaining a better understanding of the layer structures and deformation regimes in the deep sections of polar ice sheets, this work investigated the lowermost 20% of the DF ice core using innovative analytical methods. Based on the Laue X-ray diffraction method, detailed information was obtained concerning the c- and a-axes of individual crystal grains while microstructural observations were used to assess migration recrystallization and potentially nucleated grains. The DTM, applied to acquire c-axis fabric data with high sampling frequency, spatial resolution and continuity, revealed large and small variations of the c-axis cluster strength and the controlling factors of them. By combining the data from DTM and Laue X-ray diffraction method allowed the crystal orientation fabric layering to be elucidated. The primary strain

configurations in the ice were found to transition from vertical compression to a combination of vertical compression and simple shear. Insoluble particles such as dust were determined to affect the fabric evolution ~~this process~~ by shifting from promoting the slower formation of c-axis clustering to inhibiting relaxation of the c-axis. The activity of dynamic recrystallization was also determined to increase from less active to more active states. The primary conclusions obtained from this work are as follows.

(i) **Development of c-axis clustering and layered structures:** The clustering strength of the single-pole c-axis fabric reached a maximum between 2400 and 2640 m. The fluctuations in cluster strength increased substantially below this depth. Up to a depth of 2700 m, the angles of inclination of the c-axes cluster and visible layers were approximately consistent but deviated from the vertical. The system rotated as a rigid body as a result of simple shear strain while the c-axes cluster alone rotated backward because of the compression components of the simple shear applied to the ice. The primary role of shear stress in the deep sections was similar to the effects observed in the EDML ice core (Weikusat et al., 2017).

(ii) **The similarity between the DF and EDC ice cores:** The general trends exhibited by the c-axis cluster strength and grain sizes in the present work were approximately the same as those seen in the EDC ice core (Durand et al. 2009). These similarities may be attributed to equivalent impurity concentration profiles (which in turn are associated with climate change) and temperature profiles. Hence, it appears that rigid body rotation does not affect cluster strength.

(iii) **The preferred a-axis fabric:** The a-axis fabric exhibited a preferred orientation within the plane of the a-axis girdle on the spatial scale of the thin sections used for the Laue measurements. This organization of the preferred a-axis fabric was enhanced in impurity-poor ice.

(iv) **Roles of nucleation and migration recrystallization:** Evidence of migration recrystallization, such as bulged grain boundaries and interlocking grains, as well as potentially nucleated grains, were found in impurity-poor layers. These microstructures were unique to deeper sections. It appears that nucleation and migration recrystallization lead to the c-axis relaxation and a-axis organization observed in this work.

(v) **Contrast between impurity-rich and impurity-poor layers:** The relationship between cluster strength and the concentration of dusty impurities was found to change at approximately 2640 m. Below this depth, layers having higher concentrations of impurities were found to maintain stronger c-axis clustering and smaller grain sizes. In contrast, impurity-poor layers exhibited relaxation of c-axis clustering and increased crystal sizes due to nucleation and migration recrystallization. These effects modified both the c-axis and a-axis fabric of such layers.

(vi) **Grain sizes in the deepest sections:** Small grain sizes were maintained between 2900 and 2950 m. Grain boundary pinning by insoluble impurities remained significant even at high temperatures close to the melting point of ice. However, the grain sizes became extremely large below 2960 m. In the high temperature environment near the bedrock, small variations in the concentration of impurities greatly affected the microstructure.

Data availability

The data used in this paper will be published in the National Institute of Polar Research ADS data repository in conjunction with the publication of the present manuscript in The Cryosphere.

Author contributions

Author contributions are listed herein using the CrediT system (Ghan et al., 2016) to provide greater clarity concerning these contributions. TS: Conceptualization, Methodology, Validation, Formal analysis, Investigation, Data curation, Writing - Original draft, Visualization. AM: Conceptualization, Methodology, Validation, Formal analysis, Investigation, Data curation, Writing - Review & editing, Visualization. SF: Conceptualization, Methodology, Validation, Formal analysis,

534 Investigation, Writing - Original draft, Supervision, Project administration, Funding acquisition. TK: Investigation, Writing -
535 Review & editing. MI: Investigation. KG-A, MH, AH, YI, HO, WS and ST: Writing - Review & editing.

536 *Competing interests*

537 The authors declare that they have no conflict of interests.

538 *Acknowledgements*

539 The authors thank the handling editor Mathieu Casado and Maurine Montagnat, David Prior and two anonymous reviewers
540 for helpful comments and suggestions. The authors are grateful to all the Dome Fuji Deep Ice Core Project Members who
541 contributed to obtaining the ice core samples, either through logistics, drilling or core processing. Primary logistics support
542 was provided by the Japanese Antarctic Research Expedition (JARE), managed by the Ministry of Education, Culture,
543 Sports, Science and Technology (MEXT). This work was supported by JSPS KAKENHI Grant Number 18H05294.

544

Appendix A: Microstructures: Results and interpretations

A1 Microstructural features in glacial and interglacial periods

The present study provides limited but significant examples of noteworthy microstructures, as shown in Figures A1 and A2. In Figure A1, five examples are provided that include impurity-rich ice (panel a: 2648 m, ~270 ppbv dust concentration; panel c: 2759 m, ~137 ppbv), impurity-poor ice (panel b: 2685 m, ~10 ppbv; panel d: 2872 m, ~3 ppbv) and impurity-rich deep ice (panel e: 2907.5 m, ~80 ppbv). Images are presented of thin sections viewed through crossed polaroids together with c-axis fabric data for each grain obtained using the G50 instrument and microscopy images. The thin black lines in the microscopy images indicate grain boundaries. Such boundaries when on the reverse side of a thin section appear as thinner lines. Illustrations of the front and reverse side grain boundaries and the subgrain boundaries are provided in Figure S3 in Supplementary Information Section 1.5. Panels (a) and (c) show numerous small grains with c-axis orientations that are obviously offset from the vertical direction (see the c-axis fabric image). These grains are sparsely distributed, and typically have sizes on the order of a millimetre or less. Flattened (or two-dimensionally elongated) grains having a noticeable slant are also evident. These features were present in the impurity-rich depths but absent at impurity-poor depths. In the case of panels (b) and (d), much coarser grains are apparent with a c-axis orientation distinctly offset from the vertical direction. Compared with the results for the impurity-rich layers, these coarser grains occupy much larger areas in the image, having diameters of several millimetres. In the case of the two deepest samples (panels (d) and (e)), it is evident that the crystal grain boundaries often appear as straight lines with few subgrain boundaries. Panel (e) shows an impurity-rich layer, in which the crystal grains are coarser relative to those in (a) and (c). Furthermore some characteristics of the impurity-rich layers in panels (a) and (c) are less pronounced in (e).

The $\Delta\varepsilon$ values were affected by the volume fraction of grains having a c-axis orientation that was significantly offset from the surrounding grains. In this regard, the coarser grains also had a greater effect compared with the more sparsely distributed smaller grains. Because the $\Delta\varepsilon$ values represented volume-weighted averages within the microwave beam, these values were decreased to a greater extent in the case that more and/or larger grains with c-axis orientations distinctly offset from the surrounding grains were present.

1. Polarized images **2. *c*-axis fabric images** **3. Optical microscopy images**

(a) 2648 m: impurity-rich ice
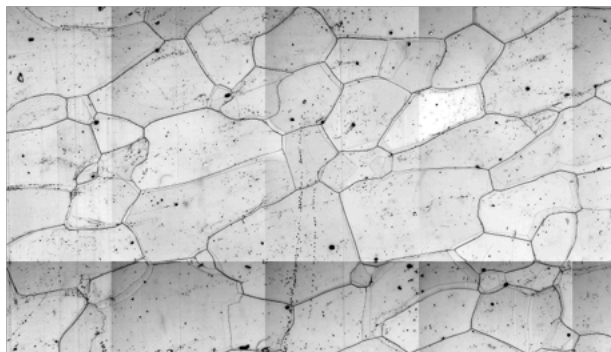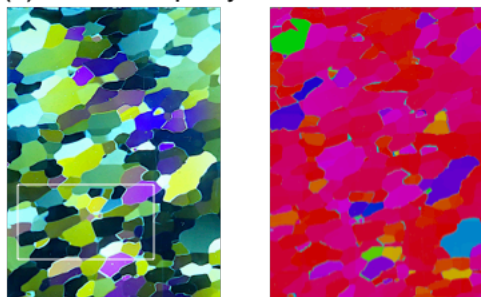
(b) 2685 m: impurity-poor ice (interglacial)
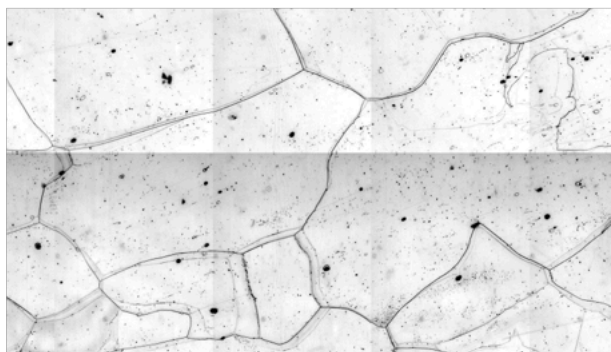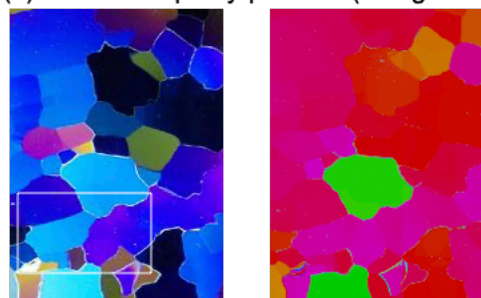
(c) 2759 m: impurity-rich ice
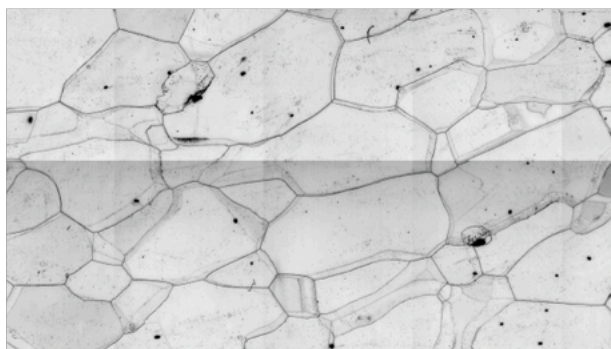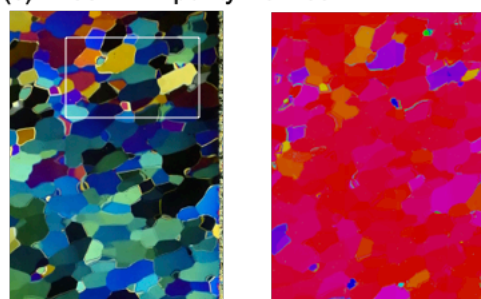
(d) 2872 m: impurity-poor ice (interglacial)
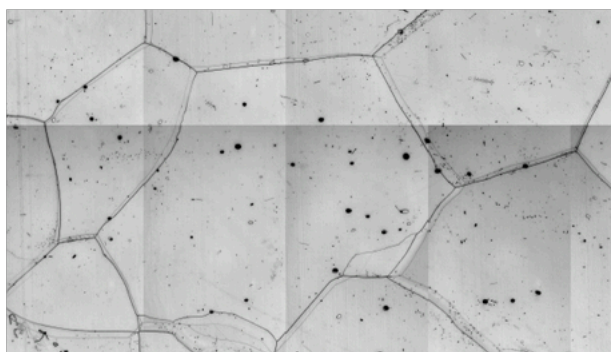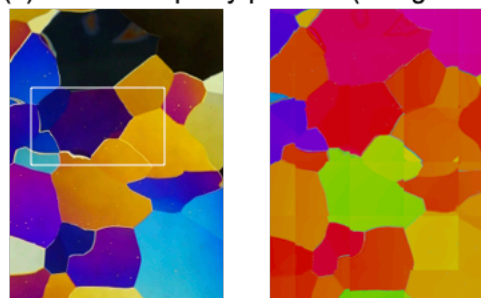
(e) 2907.5 m: impurity-rich ice
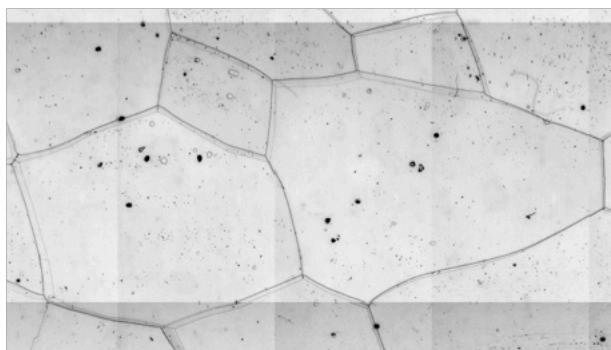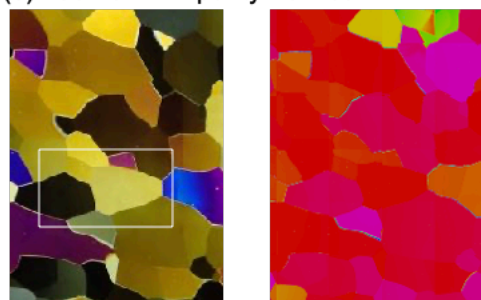
10 mm   *c*-axis orientation   2 mm

Figure A1. Microstructure images of typical specimens from five depths. The depths and ice type for each specimen are specified in the figure. For each depth, an image of a thin section viewed through crossed polaroids (left), a *c*-axis fabric image (centre) and optical

microscopy images (right) are presented. In the optical microscopy images, the thin black lines indicate grain boundaries while grain boundaries on the reverse side of the sample are visible as thinner lines. The white rectangles in the leftmost column indicate the locations from which the microscopy images shown in the right column were obtained. A legend concerning the colour coding of the *c*-axis orientation data in the images in the central column is provided at the base of the figure. The colour of each grain indicates the orientation of the *c*-axis, with red showing a vertical orientation.

A2 Microstructures in the impurity-rich layer: grain elongation ~~and smaller grain sizes~~

Remarkably, the crystal grains in the impurity-rich layers were often flattened and the major axes of these grains were inclined away from the horizontal. These features were not identified in the surrounding impurity-poor (interglacial) layers. An example of the slanting and flattened grains is shown in Figure A2a. To better assess this grain flattening, the aspect ratios based on the long and short axes of a two-dimensional fitted ellipse were analysed using the ImageJ software package. These aspect ratios were found to differ significantly between the impurity-rich and impurity-poor layers, with values in the ranges of 1.9–2.0 and 1.5–1.7, respectively. More detailed data are provided in Table S4 in Supplementary Information Section 1.5.

A similar two-dimensional feature, known as the "brick-wall pattern," has been reported to occur in layers having high concentrations of impurities from the Antarctic EDML ice core (Faria, 2009) but this phenomenon has not yet been observed in the Antarctic EDC ice core. Kuiper et al. (2020) found fine-grained bands with flattened (or elongated in two dimensions) grains having an aspect ratio of 2 in the Greenland NEEM ice core. This aspect ratio was as large as the maximum value observed in the DF core specimens. Weikusat et al. (2017) suggested that shear deformation was responsible for the flattened or elongated grains identified in the EDML core, while Faria et al. (2009) proposed that deformation via microscopic grain boundary sliding via microshear generated the brick-wall pattern. According to these prior studies, grain boundary sliding is likely promoted by a combination of smaller grain sizes, the presence of moderate stress, and higher temperatures. Smaller grain sizes often occur in the presence of high concentrations of impurities and these conditions are typically found in impurity-rich layers in the deeper sections of ice sheets (Faria et al. 2009). Grain elongation becomes less pronounced in more deeper sections, as shown in Figure A1e, which provides data for a sample from a depth of 2907.5 m. The authors suggest that the flattened features were maintained but were reduced by recovery and recrystallization processes occurring at high temperatures close to the melting point of ice. The extent of flattening could be determined by the temperature of the ice, and thus the depth, and by the impurity concentration.

A3 Migration recrystallization and grain nucleation

In dynamic recrystallization processes, rotation recrystallization has a minimal effect on the *c*-axis fabric but reduces both the grain size and aspect ratio. In contrast, migration recrystallization can significantly modify the *c*-axis fabric (e.g., De La Chapelle et al., 1998; Cuffey and Paterson, 2010). In the case that several neighbouring grains contain different amounts of stored strain energy, the grain boundary will migrate towards the higher-energy grain (e.g., Faria et al., 2014b). During this strain-induced migration recrystallization, grain boundaries sometimes become irregular and form interlocking patterns (Duval and Castelnau, 1995; Faria et al., 2014b). Figures A2b and A2c show a specimen from a depth of 2685 m with features presumably resulting from strain-induced migration recrystallization. In panel (b), the large grain in the upper left (b1) exhibits a convex grain boundary with the adjacent grain (b2) whereas, in panel (c), the lower grain (c1) has a convex grain boundary with the adjacent grain (c3). The presence of numerous subgrain boundaries implies a region of high strain that is heterogeneously dispersed (Faria et al., 2014b; Stoll et al., 2021a). Interlocking grains are evident in Figure A2d, which presents images for a sample from a depth of 2872 m. Here, grains having various *c*-axis orientations are intricately interwoven (see the *c*-axis fabric image). It should also be noted that these features were found in impurity-poor layers.

Grain nucleation in ice is thought to occur at triple junctions and at grain boundaries or similar regions characterized by high concentration of dislocation walls and subgrain boundaries (Faria et al. 2014b). The authors note that it is very challenging to identify a grain immediately following nucleation, as this requires a series of observations over time. The grain may grow immediately after nucleation in natural ice samples and so observation can be difficult. ~~However, considering the morphological features of the small grains with a *c*-axis distinctly offset from that of surrounding larger grains (Figures A1a, A1c and A2a), these grains may have been nucleated at some point during the deformational history of the ice within the sheet.~~ Although there have been several studies investigating grain nucleation in artificially deformed ice (e.g., Montagnat et al., 2015; Chauve et al., 2017), there have been few reports of this process in natural ice samples. Faria et al. (2014b) suggested that a nucleated grain will not exhibit internal structures but will bulge toward a region rich in dislocation walls and subgrain boundaries. Examples of grains with such features are shown in Figures A2e and A2f. Here, small grains with no internal structures (e1 and f1) can be seen to be situated at grain boundaries. These grains have *c*-axis orientations close to those of the adjacent grains (e2 and f2) (see the *c*-axis fabric images in panels e and f). Considering the morphological features of the small grains, these grains may have been nucleated at some point during the deformational history of the ice within the sheet.

Dust particle segregation was found to be associated with grain boundary migration (Figure A2g). Note that, in this figure, the thin lines adjacent to the grain boundary represent the reverse side of the grain boundary and indicate that dust particles were segregated along the planes of the crystal grains. Grain boundary migration in the deeper parts of the ice core likely promoted the redistribution of soluble impurities and dust particles.
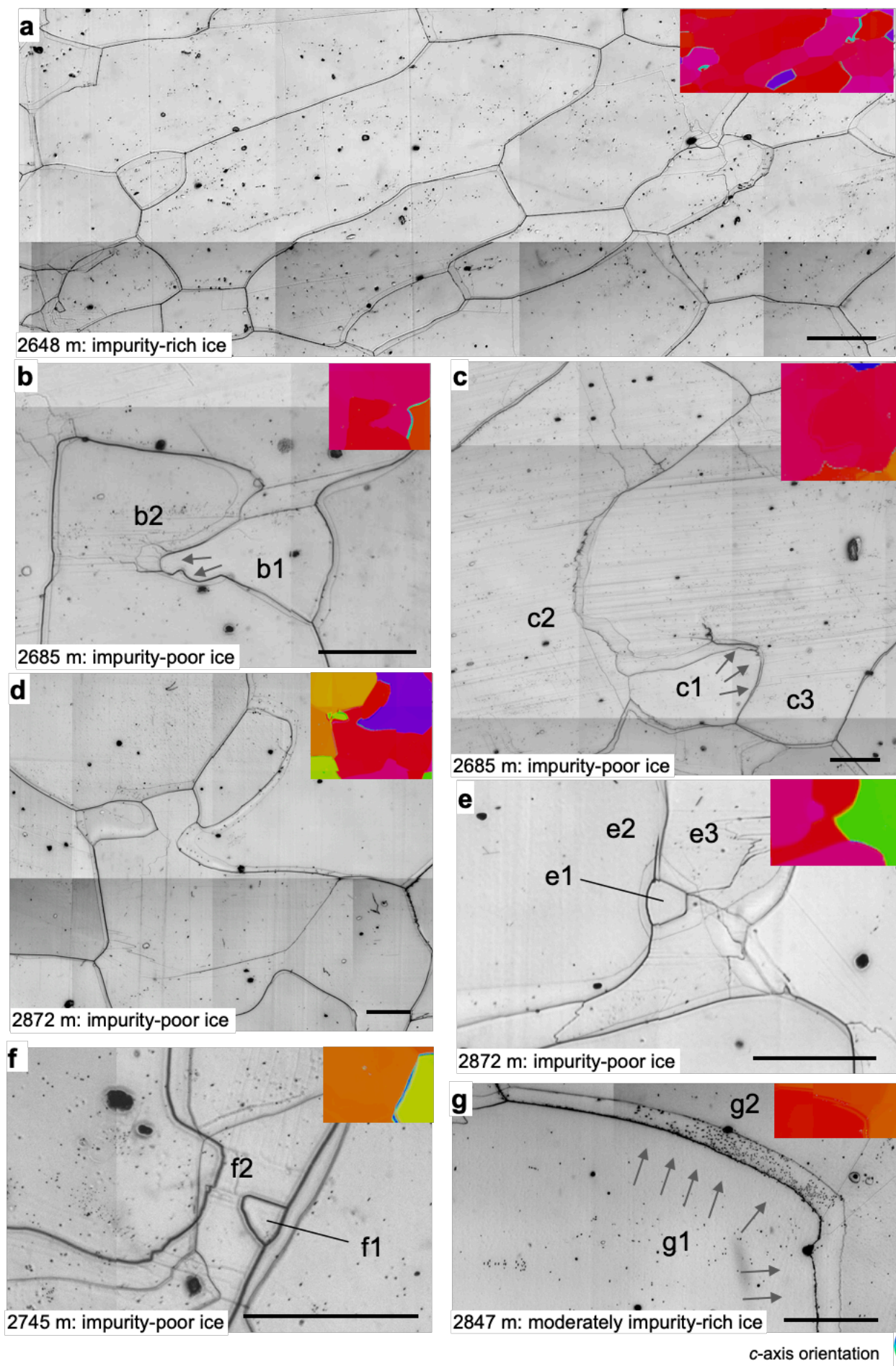
Figure A2. Images of microstructures in specimens from five depths showing grain elongation and migration recrystallization. The depths are indicated in each panel and also summarized at the top of Figure 5. All images were acquired from vertical thin sections. The solid

black lines indicate grain boundaries while grain boundaries on the reverse side of each section are visible as thin lines. The arrows indicate convex grain boundaries. Colour coding of the c-axis fabric image in each panel indicates the c-axis orientation of each grain and the accompanying legend is displayed at the bottom right. Grains shown in red and green/blue have the c-axis oriented vertically and horizontally, respectively. (a) Flattened (or elongated in two dimensions) and slanting grains observed in the impurity-rich layer. (b) and (c) Typical results from a depth of 2685 m. (b) The small grain (b1) with bulging (cuspidate) grain boundaries. (c) The lower grain (c1) with bulging (cuspidate) grain boundaries. (d) An example of interlocking grains in a sample from a depth of 2872 m. Grains with various c-axis orientations are intricately interwoven. (e) and (f) Possible examples of grain nucleation in samples from depths of 2872 and 2745 m. The small grains (e1 and f1) exhibit a lack of internal structures such as slip bands and subgrain boundaries, while the adjacent grains display many slip bands and subgrain boundaries. (g) The segregation of dust particles along the front of a grain boundary in a sample from a depth of 2847 m. Scale bars: 2 mm.

References

Alley, R.B.: Flow law hypotheses for ice sheet modelling, J. Glaciol., 38(12), 245–256, https://doi.org/10.3189/S0022143000003658, 1992.

Alley, R. B., and Woods, G. A.: Impurity influence on normal grain growth in the GISP2 ice core, Greenland, J. Glaciol., 42(141), 255–260, https://doi.org/10.3189/S0022143000004111, 1996.

Azuma, N., Wang, Y., Mori, K., Narita, H., Hondoh, T., Shoji, H., and Watanabe O.: Textures and fabrics in the Dome F (Antarctica) ice core, Ann. Glaciol., 29, 163–168, https://doi.org/10.3189/172756499781821148, 1999.

Azuma, N., Wang, Y., Yoshida, Y., Narita, H., Hondoh, T., Shoji, H., and Watanabe, O.: Crystallographic analysis of the Dome Fuji ice core, in: Physics of Ice Core Records, edited by: Hondoh, T., Hokkaido University Press, Sapporo, 45–61, 2000.

Bamber, J. L., Gomez-Dans, J. L., and Griggs, J. A.: Antarctic 1 km Digital Elevation Model (DEM) from combined ERS-1 radar and ICESat Laser satellite altimetry, in: National Snow and Ice Data Center, Digital media, Boulder, Colorado, USA, 2009.

Bazin, L., Landais, A., Lemieux-Dudon, B., Toyé Mahamadou Kele, H., Veres, D., Parrenin, F., Martinerie, P., Ritz, C., Capron, E., Lipenkov, V., Loutre, M.F., Raynaud, D., Vinther, B., Svensson, A., Rasmussen, S. O., Severi, M., Blunier, T., Leuenberger, M., Fischer, H., Masson-Delmotte, V., Chappellaz, J., and Wolff, E.: An optimized multi-proxy, multi-site Antarctic ice and gas orbital chronology (AICC2012): 120–800 ka, Clim. Past, 9(4), 1715–1731, https://doi.org/10.5194/cp-9-1715-2013, 2013.

Chauve, T., Montagnat, M., Barou, F., Hidas, K., Tommasi, A., and Mainprice, D.: Investigation of nucleation processes during dynamic recrystallization of ice using cryo-EBSD, Phil. Trans. R. Soc. A, 375, 20150345, http://dx.doi.org/10.1098/rsta.2015.0345, 2017.

Cuffey, K. M., and Paterson, W. S. B.: The Physics of Glaciers, 4th edition, Elsevier, Amsterdam, 2010.

Cullen, A. L.: Infrared and Millimeter Waves, in Millimeter-Wave Open-Resonator Techniques, Academic Press, New York, pp. 233–280, 1983.

De La Chapelle, S., Castelnau, O., Lipenkov, V., and Duval, P.: Dynamic recrystallization and texture development ice as revealed by the study of deep ice cores Antarctica and Greenland, J. Geophys. Res., 103, 5091–5105, https://doi.org/10.1029/97JB02621, 1998.

Dome Fuji Ice Core Project Members: State dependence of climatic instability over the past 720,000 years from Antarctic ice cores and climate modeling, Sci. Adv., 3(2), e1600446, https://doi.org/10.1126/sciadv.1600446, 2017.

Durand, G., Weiss, J., Lipenkov, V., Barnola, J., Krinner, G., Parrenin, F., Delmonte, B., Ritz, C., Duval, P., and Röthlisberger, R.: Effect of impurities on grain growth in cold ice sheets, J. Geophys. Res., 111(F1)., F01015, https://doi.org/10.1029/2005JF000320, 2006.

Durand, Gillet-Chaulet, F., Svensson, A., Gagliardini, O., Kipfstuhl, S., Meyssonnier, J., Parrenin, F., Duval, P., and Dahl-Jensen, D.: Change in ice rheology during climate variations - implications for ice flow modelling and dating of the EPICA Dome C core, Clim. Past, 3, 155-167, https://doi.org/10.5194/cp-3-155-2007, 2007.

Durand, G., Svensson, A., Persson, A., Gagliardini, O., Gillet-Chaulet, F., Sjolte, J., Montagnat M., Dahl-Jensen, D.: Evolution of the texture along the EPICA Dome C ice core, in: Physics of Ice Core Records II, edited by: Hondoh, T., Hokkaido University Press, Sapporo, 91–105, 2009.

Duval, P., Ashby, M. F., and Anderman, I.: Rate-controlling pro- cesses in the creep of polycrystalline ice, J. Phys. Chem., 87, 4066–4074, https://doi.org/10.1021/j100244a014, 1983.

Duval, P. and Castelnau, O.: Dynamic recrystallization of ice in polar ice sheets, J. Phys. III, 5, 197–205, https://doi.org/10.1051/jp4:1995317, 1995.

Eichler, J., Kleitz, I., Bayer-Giraldi, M., Jansen, D., Kipfstuhl, S., Shigeyama, W., Weikusat, C., and Weikusat, I.: Location and distribution of micro-inclusions in the EDML and NEEM ice cores using optical microscopy and in situ Raman spectroscopy, The Cryosphere, 11, 1075-1090, https://doi.org/10.5194/tc-11-1075-2017, 2017.

Eisen, O., Steinhage, D., Karlsson, N. B., Binder, T., Helm, V.: Ice thickness of Dome Fuji region, Antarctica, recorded with the AWI airborne radar system: line 20172048. PANGAEA, https://doi.org/10.1594/PANGAEA.920649, 2020.

EPICA Community Members: Eight glacial cycles from an Antarctic ice core, Nature, 429, 623–628, https://doi.org/10.1038/nature02599, 2004.

Faria, S. H., Kipfstuhl, S., Azuma, N., Freitag, J., Weikusat., I., Murshed, M. M., and Kuhs, W. F.: The Multiscale Structure of Antarctica Part I: Inland Ice, in: Physics of Ice Core Records II, edited by: Hondoh, T., Hokkaido University Press, Sapporo, 39–59, 2009.

Faria, S. H., Weikusat, I., and Azuma, N.: The microstructure of polar ice. Part I: Highlights from ice core research, J. Struct. Geol., 61, 2–20, http://dx.doi.org/10.1016/j.jsg.2013.09.010, 2014a.

Faria, S. H., Weikusat, I., and Azuma, N.: The microstructure of polar ice. Part II: State of the art, J. Struct. Geol., 61, 21–49, http://dx.doi.org/10.1016/j.jsg.2013.11.003, 2014b.

Fujita, S., Maeno, H., and Matsuoka, K.: Radio-wave depolarization and scattering within ice sheets: a matrix-based model to link radar and ice-core measurements and its application, J. Glaciol., 52, 407-424, https://doi.org/10.3189/172756506781828548, 2006

Fujita, S., Okuyama, J., Hori, A., and Hondoh, T.: Metamorphism of stratified firn at Dome Fuji, Antarctica: A mechanism for local insolation modulation of gas transport conditions during bubble close off, J. Geophys. Res., 114, F03023, https://doi.org/10.1029/2008JF001143, 2009.

Fujita, S., Holmlund, P., Andersson, I., Brown, I., Enomoto, H., Fujii, Y., Fujita, K., Fukui, K., Furukawa, T., Hansson, M.,Hara, K., Hoshina, Y., Igarashi, M., Iizuka, Y., Imura, S., Ingvander, S., Karlin, T., Motoyama, H., Nakazawa, F., Oerter, H., Sjöberg, L. E., Sugiyama, S., Surdyk, S., Ström, J., Uemura, R., and Wilhelms, F.: Spatial and temporal variability of snow accumulation rate on the East Antarctic ice divide between Dome Fuji and EPICA DML, The Cryosphere, 5, 1057–1081, https://doi.org/10.5194/tc-5-1057-2011, 2011.

Fujita, S., Holmlund, P., Matsuoka, K., Enomoto, H., Fukui, K., Nakazawa, F., Sugiyama, S., and Surdyk, S.: Radar diagnosis of the subglacial conditions in Dronning Maud Land, East Antarctica, The Cryosphere, 6, 1203–1219, https://doi.org/10.5194/tc-6-1203-2012, 2012.

Fujita, S., Hirabayashi, M., Goto-Azuma, K., Dallmayr, R., Satow, K., Zheng, J., and Dahl-Jensen, D.: Densification of layered firn of the ice sheet at NEEM, Greenland, J. Glaciol., 60, 905-921, https://doi.org/10.3189/2014JoG14J006, 2014.

Fujita, S., Goto-Azuma, K., Hirabayashi, M., Hori, A., Iizuka, Y., Motizuki, Y., Motoyama H., and Takahashi, K.: Densification of layered firn in the ice sheet at Dome Fuji, Antarctica, J. Glaciol., 62(231), 103–123, https://doi.org/10.1017/jog.2016.16, 2016.

Ghan, S., Crawford, J., Langematz, U., Leung, R., Li, Z., Russell, L., Steiner, A., and Zhang, C.: Author contributions can be clarified, J. Geophys. Res., 121, 8155–8155, https://doi.org/10.1002/2016JD025417, 2016.

Goodman, D. J., Frost, H. J., and Ashby, M. F.: The plasticity of polycrystalline ice, Philos. Mag., 43(3), 665–695, https://doi.org/10.1080/01418618108240401, 1981.

Goto-Azuma, K., Hirabayashi, M., Motoyama, H., Miyake, T., Kuramoto, T., Uemura, R., Igarashi, M., Iizuka, Y., Sakurai, T., and Horikawa, S.: Reduced marine phytoplankton sulphur emissions in the Southern Ocean during the past seven glacials, Nat. Commun., 10(1): 1–7, https://doi.org/10.1038/s41467-019-11128-6, 2019.

Hargreaves, N. D.: The radio-frequency birefringence of polar ice, J. Glaciol, 21(85), 301–313, https://doi.org/10.3189/S0022143000033499, 1978.

Humphreys, F. and Hatherly, M.: Recrystallization and Related Annealing Phenomena, 2nd edn., Elsevier, https://doi.org/10.1016/B978-0-08-044164-1.X5000-2, 2004.

Inoue, R., Fujita, S., Kawamura, K., Oyabu, I., Nakazawa, F., Motoyama, H., and Aoki, T.: Spatial distribution of vertical density and microstructure profiles in near-surface firn around Dome Fuji, Antarctica, The Cryosphere, 18, 425–449, https://doi.org/10.5194/tc-18-425-2024, 2024.

Jacka, T. and Li, J.: The steady-state crystal size of deforming ice, Ann. Glaciol., 20, 13–18, https://doi.org/10.3189/1994AoG20-1-13-18, 1994.

Jones, R. G.: The measurement of dielectric anisotropy using a microwave open resonator, J. Phys. D: Applied Physics, 9(5), 819–827, https://doi.org/10.1088/0022-3727/9/5/015, 1976a.

Jones, R. G.: Precise dielectric measurements at 35 GHz using an open microwave resonator, Proc. IEEE, 123(4), 285–290, http://doi.org/10.1049/piee.1976.0067, 1976b.

Kipfstuhl, S., Faria, S. H., Azuma, N., Freitag, J., Hamann, I., Kaufmann, P., Miller, H., Weiler, K., and Wilhelms, F.: Evidence of dynamic recrystallization in polar firn, J. Geophys. Res., 114, B05204, https://doi.org/10.1029/2008JB005583, 2009.

Komiyama, B., Kiyokawa, M., and Matsui, T.: Open resonator for precision dielectric measurements in the 100 GHz band. IEEE Trans. Microw. Theory Tech., 30(10), 1792–1796, https://doi.org/10.1109/22.88556, 1991.

Kuiper, E.-J. N., Weikusat, I., de Bresser, J. H. P., Jansen, D., Pennock, G. M., and Drury, M. R.: Using a composite flow law to model deformation in the NEEM deep ice core, Greenland – Part 1: The role of grain size and grain size distribution on deformation of the upper 2207 m, The Cryosphere, 14, 2429–2448, https://doi.org/10.5194/tc-14-2429-2020, 2020.

Langway, C. C.: Ice fabrics and the universal stage, SIPRE Tech. Rep., 62, 1958.

Matsuoka, T., Mae, S., Fukazawa, H., Fujita, S., and Watanabe, O.: Microwave dielectric properties of the ice core from Dome Fuji, Antarctica, Geophys. Res. Lett., 25, 1573–1576, https://doi.org/10.1029/98GL01225, 1998.

Miyamoto, A., Weikusat, I., and Hondoh, T.: Complete determination of ice crystal orientation using Laue X-ray diffraction method. J. Glaciol., 57(201), 103–110, https://doi.org/10.3189/002214311795306754, 2011.

Montagnat, M., Durand, G., and Duval, P.: Recrystallization processes in granular ice, in: Physics of Ice Core Records II, edited by: Hondoh, T., Hokkaido University Press, Sapporo, 81–90, 2009.

Montagnat, M., Buiron, D., Arnaud, L., Broquet, A., Schlitz, P., Jacob, R., and Kipfstuhl, S.: Measurements and numerical simulation of fabric evolution along the Talos Dome ice core, Antarctica, Earth and Planetary Science Letters, 357-358, 168-178, https://doi.org/10.1016/j.epsl.2012.09.025, 2012.

Montagnat, M., Azuma, N., Dahl-Jensen, D., Eichler, J., Fujita, S., Gillet-Chaulet, F., Kipfstuhl, S., Samyn, D., Svensson, A., and Weikusat, I.: Fabric along the NEEM ice core, Greenland, and its comparison with GRIP and NGRIP ice cores, The Cryosphere, 8, 1129-1138, https://doi.org/10.5194/tc-8-1129-2014, 2014.

Montagnat, M., Chauve, T., Barou, F., Tommasi, A., Beausir, B., and Fressengeas, C.: Analysis of Dynamic Recrystallization of Ice from EBSD Orientation Mapping, Front. Earth Sci., 3, 81, https://doi.org/10.3389/feart.2015.00081, 2015.

Motoyama, H., Takahashi, A., Tanaka, Y., Shinbori, K., Miyahara, M., Yoshimoto, T., Fujii, Y., Furusaki, A., Azuma, N., and Ozawa, Y.: Deep ice core drilling to a depth of 3035.22 m at Dome Fuji, Antarctica in 2001–07, Ann. Glaciol., 62(85-86), 212–222, https://doi.org/10.1017/aog.2020.84, 2020.

Ohno, H., Iizuka, Y., Hori, A., Miyamoto, A., Hirabayashi, M., Miyake, T., Kuramoto, T., Fujita, S., Segawa, T., Uemura, R., Sakurai, T., Suzuki, T., and Motoyama, H.: Physicochemical properties of bottom ice from Dome Fuji, inland East Antarctica, J. Geophys. Res., 121(7), 1230–1250, https://doi.org/10.1002/2015JF003777, 2016.

Oyabu, I., Kawamura, K., Fujita, S., Inoue, R., Motoyama, H., Fukui, K., Hirabayashi, M., Hoshina, Y., Kurita, N., Nakazawa, F., Ohno, H., Sugiura, K., Suzuki, T., Tsutaki, S., Abe-Ouchi, A., Niwano, M., Parrenin, F., Saito, F., and Yoshimori, M.: Temporal variations of surface mass balance over the last 5000 years around Dome Fuji, Dronning Maud Land, East Antarctica, Clim. Past, 19, 293–321, https://doi.org/10.5194/cp-19-293-2023, 2023.

Parrenin, F., Fujita, S., Abe-Ouchi, A., Kawamura, K., Masson-Delmotte, V., Motoyama, H., Saito, F., Severi, M., Stenni, B., Uemura, R., and Wolff, E. W.: Climate dependent contrast in surface mass balance in East Antarctica over the past 216 ka, Journal of Glaciology, 1-12, https://doi.org/10.1017/jog.2016.85, 2016, 2016.

Pattyn, F.: Antarctic subglacial conditions inferred from a hybrid ice sheet/ice stream model, Earth Planet. Sc. Lett., 295(3–4), 451–461, https://doi.org/10.1016/j.epsl.2010.04.025, 2010.

Petrenko, V. F., and Whitworth, R. W.: Physics of Ice, Oxford University Press, Oxford, 1999.

Poirier J.-P. 1985. Creep of Crystals. Cambridge Earth Science Series. Xiv, Cambridge University Press. ISBN 0 521 26177, Geological Magazine, 122, 579-580, https://doi.org/10.1017/S0016756800035664, 1985.

Russell-Head, D. S. and Budd, W. F.: Ice-sheet flow properties derived from bore-hole shear measurements combined with ice-core studies, J. Glaciol., 24, 117-130, https://doi.org/10.3189/S0022143000014684, 1979.

Saruya, T., Fujita, S., and Inoue, R.: Dielectric anisotropy as indicator of crystal orientation fabric in Dome Fuji ice core: method and initial results, J. Glaciol., 68(267), 65–76, https://doi.org/10.1017/jog.2021.73, 2022a.

Saruya, T., Fujita, S., Iizuka, Y., Miyamoto, A., Ohno, H., Hori, A., Shigeyama, W., Hirabayashi, M., and Goto-Azuma, K.: Development of crystal orientation fabric in the Dome Fuji ice core in East Antarctica: implications for the deformation regime in ice sheets, The Cryosphere 16(7), 2985–3003, https://doi.org/10.5194/tc-16-2985-2022, 2022b.

Shoji, H., and Higashi, A.: A deformation mechanism map of ice, J. Glaciol., 85(21), 419–427, https://doi.org/10.3189/S002214300003358X, 1978.

Steinbach, F., Kuiper, E.-J. N., Eichler, J., Bons, P. D., Drury, M. R., Griera, A., Pennock, G. M., and Weikusat, I.: The Relevance of Grain Dissection for Grain Size Reduction in Polar Ice: Insights from Numerical Models and Ice Core Microstructure Analysis, Front. Earth Sci., 5, https://doi.org/10.3389/feart.2017.00066, 2017.

Stoll, N., Eichler, J., Hörhold, M., Erhardt, T., Jensen, C., and Weikusat, I.: Microstructure, micro-inclusions, and mineralogy along the EGRIP ice core – Part 1: Localisation of inclusions and deformation patterns, The Cryosphere, 15, 5717–5737, https://doi.org/10.5194/tc- 15-5717-2021, 2021a.

Stoll, N., Eichler, J., Hörhold, M., Shigeyama, W., and Weikusat, I.: A Review of the Microstructural Location of Impurities in Polar Ice and Their Impacts on Deformation, Front. Earth Sci., 8, 615613, https://doi.org/10.3389/feart.2020.615613, 2021b.

Stoll, N., Hörhold, M., Erhardt, T., Eichler, J., Jensen, C., and Weikusat, I.: Microstructure, micro-inclusions, and mineralogy along the EGRIP (East Greenland Ice Core Project) ice core – Part 2: Implications for palaeo-mineralogy, The Cryosphere, 16, 667–688, https://doi.org/10.5194/tc-16-667-2022, 2022.

Thorsteinsson, T., Kipfstuhl, J. and Miller, H.: Textures and fabrics in the GRIP ice core, J. Geophys. Res., 102(C12), 26583–26599, https://doi.org/10.1029/97JC00161, 1997.

Tsutaki, S., Fujita, S., Kawamura, K., Abe-Ouchi, A., Fukui, K., Motoyama, H., Hoshina, Y., Nakazawa, F., Obase, T., Ohno, H., Oyabu, I., Saito, F., Sugiura, K., and Suzuki, T.: High-resolution subglacial topography around Dome Fuji, Antarctica, based on ground-based radar surveys conducted over 30 years, The Cryosphere, 16, 2967–2983, https://doi.org/10.5194/tc-16-2967-2022, 2022.

Weikusat, I., Kipfstuhl, S., Faria, S. H., Azuma, N., and Miyamoto, A.: Subgrain boundaries and related microstructural features in EDML (Antarctica) deep ice core, J. Glaciol., 55, 461-472, https://doi.org/10.3189/002214309788816614, 2009.

813 Weikusat, I., Jansen, D., Binder, T., Eichler, J., Faria, S. H., Wilhelms, F., Kipfstuhl, S., Sheldon, S., Miller, H., Dahl-Jensen,
814   D., and Kleiner, T.: Physical analysis of an Antarctic ice core – towards an integration of micro- and macrodynamics of
815   polar ice, Phil. Trans. R. Soc. A, 375, 20150347, http://dx.doi.org/10.1098/rsta.2015.0347, 2017.
816 Yamanouchi, T., Hirasawa, N., Hayashi, M., Takahashi, S., and Kaneto, S.: Meteorological characteristics of Antarctic
817   inland station, Dome Fuji. Mem. Natl Inst. Polar Res., Spec. Issue, 57, 94–104, 2003.
818